Acta Pharmaceutica Sinica B 2026;16(3):1676−1695

Chinese Pharmaceutical Association
Institute of Materia Medica, Chinese Academy of Medical Sciences

Acta Pharmaceutica Sinica B

www.elsevier.com/locate/apsb
www.sciencedirect.com

ORIGINAL ARTICLE

Reversibly unlocking the blood−brain barrier: A study on microtubule dynamics modulation using gold nanoparticle-modified reduced graphene oxide

Junrong Wu[a,†], Guangman Cui[b,†], Zhousheng Lin[b,†], Wanmei Lin[b], Yaqing Zhang[a], Tianhang Zhou[e], Ping He[d,*], Yunjiao Zhang[c,*], Guangyu Yao[b,*]

[a]*Stomatological Hospital, School of Stomatology, Southern Medical University, Guangzhou 510280, China*
[b]*Breast Center, Department of General Surgery, Nanfang Hospital, Southern Medical University, Guangzhou 510515, China*
[c]*School of Medicine, South China University of Technology, Guangzhou 510006, China*
[d]*Department of Pathology, The First Affiliated Hospital of Guangzhou Medical University, Guangzhou 510120, China*
[e]*College of Carbon Neutrality Future Technology, State Key Laboratory of Heavy Oil Processing, China University of Petroleum (Beijing), Beijing 102249, China*

Received 15 May 2025; received in revised form 1 September 2025; accepted 8 September 2025

KEY WORDS

Blood−brain barrier;
Graphene-based materials;
Reduced graphene oxide;
Gold nanoparticles;
Paracellular transportation;
Microtubules;
Polymerization and depolymerization

Abstract The blood−brain barrier (BBB) is a crucial biological interface between the central nervous system and circulation, playing a key role in maintaining the brain's homeostasis and function, but presenting a challenge for drug delivery. Although enhancing the paracellular permeability of the BBB using graphene-based materials (GBMs) is a promising strategy, detailed biological effects and molecular mechanisms remain poorly understood and understudied. In this study, we prepared gold nanoparticle-modified reduced graphene oxide (Au-rGO) sheets as representative GBMs to enhance BBB paracellular permeability transiently. Remarkably, the induced permeability modulation exhibited both significant efficacy and complete reversibility. Biological experiments and molecular dynamics simulations provided full insights into the molecular mechanism of this process, confirming that Au-rGO influences the dynamic equilibrium of MTs by adsorbing soluble tubulins to hinder MT polymerization, and disassembling

*Corresponding authors.
E-mail addresses: yaogy@smu.edu.cn (Guangyu Yao), zhangyunjiao@scut.edu.cn (Yunjiao Zhang), hp5567@163.com (Ping He).
[†]These authors made equal contributions to this work.

Peer review under the responsibility of Chinese Pharmaceutical Association and Institute of Materia Medica, Chinese Academy of Medical Sciences.

https://doi.org/10.1016/j.apsb.2025.12.015

dynamics;
ERK−Stathmin pathway

MTs to promote depolymerization, thus mediating the unlocking of the BBB. Moreover, the subsequent closure of the BBB is mediated by increased MT polymerization, regulated by the activation of the ERK−stathmin pathway. Collectively, this present study comprehensively elucidates the phenomenon of reversible BBB opening induced by Au-rGO and its intricate molecular mechanism, and supports the safety and efficacy of Au-rGO as a paracellular penetration enhancer for enhancing BBB drug delivery efficiency.

1. Introduction

The blood−brain barrier (BBB) is a complex, multicellular, and dynamic interface that regulates the movement of specific biological substances essential for brain homeostasis and neuronal function. Additionally, it serves as a protective shield, preventing the brain parenchyma from exposure to harmful blood-borne agents and external compounds[1,2]. However, this tightly sealed barrier poses a significant impediment to the entry of certain drugs into the brain, whereby nearly 98% of small molecule drugs and virtually all large molecule drugs cannot pass through the BBB to penetrate the brain[3]. Among the few therapeutics that have succeeded in breaching the BBB, substantial challenges arise during clinical application, including limited capacity for effective penetration into brain tissues and BBB integrity disruption[4].

Enhancing drug penetration across the BBB primarily involves two routes: the transcellular route (transcytosis, receptor-mediated transport, or diffusion), and the paracellular route governed by adherens junctions (AJs) and tight junctions (TJs)[5]. In recent decades, the concept of leveraging nanomedicines to overcome the BBB has garnered increasing interest[6,7]. This stems from their ability to selectively target specific tissues and cells, as well as their inherent multifunctionality, which is tunable based on material composition and size[8]. The diverse range of nanomaterials crosses the BBB *via* established transport mechanisms. Nanomaterial-mediated transcellular delivery typically employs polymer micelles[9,10], liposomes[11,12] and biomimetic modification nanomaterials[13,14]; however, its key challenge lies in enhancing drug endocytosis and endosomal escape to improve delivery efficiency. While generally safe, the transcellular route offers limited permeability enhancement, particularly for large hydrophobic drugs (proteins, peptides, etc.)[3]. In contrast, opening of the paracellular route holds significant promise for substantially improving BBB permeability, enabling the entry of hydrophilic drugs with higher molecular weights into the brain[15]. Numerous studies have confirmed that nanomaterials like carbon-based nanomaterials[16] and metal-based nanomaterials[17] can influence BBB permeability, particularly by opening the paracellular route to enhance drug delivery efficiency. However, if the paracellular route fails to reseal promptly and restore the BBB's complete barrier function, it poses a serious threat to the stability and safety of the nervous system[18]. Therefore, when developing nanomaterials to function as drug carriers or paracellular penetration enhancers for BBB drug delivery, two critical metrics must be ensured: delivery efficiency (barrier opening) and safety (barrier resealing).

Graphene-based materials (GBMs) have been gaining significant attention as potential drug carriers for the treatment of central nervous system diseases due to their biocompatibility and impressive cargo-carrying capacity[19,20]. Present studies have predominantly focused on the therapeutic effects of composite nanomedicines comprising GBMs as a drug carrier[21-25]. However, few studies have systematically examined the biological effects of GBMs when employed as potential barrier penetration enhancers[26,27]. Key questions remain unanswered: Through which routes do GBMs cross the highly selective BBB? Does BBB opening mediated by GBMs result in irreversible damage to barrier integrity? What molecular mechanisms govern their interactions with cerebrovascular endothelial cells? These questions remain largely unexplored and merit further investigation.

Given this, we prepared a gold nanoparticle-modified reduced graphene oxide (Au-rGO) sheet and performed both *in vivo* and *in vitro* investigations to examine the interactions between the GBMs and the BBB. Based on the following considerations, we propose that Au-rGO can serve as an ideal model material for investigating the effects of GBMs on the BBB. Reduced graphene oxide (rGO) was chosen due to its increased hydrophobicity and $\pi-\pi$ stacking interactions compared to graphene oxide (GO), rendering it less cytotoxic and more adept at drug loading[28,29]. Assessing the distribution and quantification of GBMs *in vivo* remains challenging, given their carbon-based nature, which cannot be analyzed using conventional methods like inductively coupled plasma, and their limited imaging capabilities. To overcome these limitations, we used gold nanoparticle modification as an effective solution to quantify GBMs in trace amounts and for superior biosafety. Moreover, gold nanoparticles (AuNPs) can preserve the physical and chemical properties of rGO through surface modification *via* van der Waals forces[30].

Herein, we first confirmed that Au-rGO can rapidly and reversibly unlock the BBB, suggesting its potential as a secure and efficacious paracellular permeation enhancer for the BBB. Subsequently, we uncovered and verified the mechanism underlying Au-rGO's interaction with microtubules (MTs), which interferes with their depolymerization and polymerization dynamics and is responsible for the reversible opening of the paracellular route of the BBB. To the best of our knowledge, this study represents the first to elucidate the intricate process by which a nanomaterial can reversibly open a biological barrier at the molecular level, setting a precedent for future development of nanomaterials aimed at safely enhancing BBB permeability to improve drug delivery efficacy.

2. Materials and methods

2.1. Synthesis and characterization of Au-rGO

The graphite powder (Merck 282863, Darmstadt, Germany) was used to prepare graphene oxide *via* the Hummers' method. In brief, a mixture of 20 g graphite powder, 10 g sodium nitrate, and

60 g potassium permanganate was uniformly blended and slowly added to 460 mL sulfuric acid (98%) under stirring, maintaining the reaction temperature at 10−15 °C for 3 h. The reaction system was then transferred to a 35 °C water bath and stirred for an additional 30 min. Next, 920 mL of deionized water was slowly added to the mixture, followed by transferring the system to a 99 °C water bath for another 30 min of stirring. Afterward, 3000 mL of deionized water and 20 mL of hydrogen peroxide (5%) were added to the reaction mixture. The product was filtered while hot and thoroughly washed five times with dilute hydrochloric acid (5%) and deionized water. The resulting precipitate was dried at 60 °C to obtain graphite oxide. A 100 mL solution of graphite oxide with a concentration of 1 mg/mL was prepared and ultrasonicated (100 kHz, 200 W) for 2 h to obtain the exfoliated graphene oxide. Then, a 50 μL solution of $HAuCl_4$ (Sangon Biotech A602523, Shanghai, China) with a concentration of 0.5 mol/L was added to the 100 mL graphene oxide dispersion. The pH of the mixture was adjusted to 10, and 5 g of glucose was dispersed in the solution. The system was kept in a constant temperature water bath at 30 °C for 12 h under ultrasonication (40 kHz, 50 W) to simultaneously reduce the graphene oxide and gold ions, allowing AuNPs to nucleate on the surface of graphene. The resulting product Au-rGO is centrifuged at 2800×*g*, washed multiple times, dried overnight at 50 °C, and stored for future use.

The surface topography of Au-rGO was analyzed using a scanning electron microscope (SEM) instrument (Zeiss Sigma 300, Oberkochen, Germany) and a transmission electron microscope (TEM) instrument (Thermo Scientific Talos F200iS, MA, USA). Ramman spectroscopy (Renishaw, Gloucestershire, UK) was used to measure the structural features of Au-rGO. The functional groups of Au-GO were further detected by Fourier transform infrared spectrum (Bruker TENSOR27, MA, USA). Element composition was defined using X-ray diffraction (Rigaku ULTIMA IV, Tokyo, Japan). The interplanar spacing and size distribution were analyzed using TEM (Talos F200iS, MA, USA). The size and morphology were visualized by atomic force microscopy (Bruker Dimension Edge, MA, USA). The Au-rGO sheets were suspended in phosphate-buffered saline (PBS) and endothelial culture medium at a concentration of 1 mg/mL for hydrodynamic diameter and the zeta potential assessment using dynamic light scattering on a Zetasizer instrument (Malvern Nano ZS, Worcestershire, UK). Gold weight percent was tested by inductively coupled plasma optical emission spectrometry (ICP-OES) (Agilent 720, CA, USA). To evaluate the stability of the AuNP modification, Au-rGO was dispersed (1 mg/mL) and sonicated (40 kHz, 50 W, 1 h) in PBS, freeze-dried (12 h), and then reanalyzed by ICP-OES (Agilent 720, CA, USA) and energy dispersive spectrometer mapping (Bruker Quantax 6/30, MA, USA).

2.2. Animals and treatment

C57BL/6 male mice (weight: 20−22 g) were obtained from the animal center of the authors' affiliation. To determine the effective Au-rGO dosage, 21 mice were divided into 7 groups ($n = 3$): 0, 0.5, 1, 2, 4, 6, and 8 mg/kg Au-rGO. For time-course experiments, 60 mice were divided into 12 groups ($n = 5$): control (PBS) and Au-rGO exposure groups (30 min, 1, 2, 3, 6, 9, 12 h, 1, 3, 5, and 7 days). Au-rGO was administered *via* tail intravenous injection. Weight and general conditions were monitored post-injection, and mice were subjected to Evans blue or horseradish peroxidase injections or euthanized under anesthesia for tissue collection. All procedures followed ethical guidelines (National Ethics Committee on Animal Welfare of China) and were approved by the Ethics Committee of the authors' affiliation (Approval No. L2019162).

2.3. BBB permeability test in vivo

Following Au-rGO exposure *via* intravenous injection, mice were intravenously injected with 2% Evans blue (Macklin E6135, Shanghai, China) at a dose of 4 mL/kg body weight through the tail vein to circulate for 10 min. Cardiac perfusion was then exposed under anesthesia to eliminate the tracer from the circulation. Brains were extracted for macroscopic observation. Similar to the above procedure, mice were intravenously injected with 35% horseradish peroxidase (Merck P8375, Darmstadt, Germany) at a dose of 0.2 mg/g body weight *via* the tail vein and allowed to circulate for 10 min. Subsequently, the mice were perfused with 4% paraformaldehyde. After extraction and overnight fixation, brain tissues were sectioned into 50 μm-thick coronal sections using a vibratome. The 3,3′-diaminobenzidine (DAB) solution (ZSGB-Bio ZLI-9018, Beijing, China) was used to indicate the presence of horseradish peroxidase reaction products.

2.4. Histological analysis

Brain, kidney, liver, and lung tissues were collected, fixed, and stained with hematoxylin-eosin (H&E). For brain immunofluorescence (IF) staining, CD31 antibody (Proteintech 11265-1-AP (rabbit), IL, USA; Huabio M1511-8 (mouse), Hangzhou, China) was used to mark brain vessels, glial fibrillary acidic protein (GFAP) antibody (Cell Signaling Technology 80788, MA, USA) was used to mark reactive astrocytes around brain vessels, and Albumin antibody (Proteintech 16475-1-AP, IL, USA) was used to mark Albumin extravasation around brain vessels. H&E staining images were captured using a light microscope (Olympus BX63, Tokyo, Japan) by an uninformed observer in a sample-blinded way to prevent sampling bias. Fluorescent images were captured using a laser-scanning confocal microscope (Zeiss LSM980, Oberkochen, Germany).

2.5. Inductively coupled plasma mass spectrometry (ICP-MS)

Brain, liver, and kidney tissues were pre-digested in concentrated nitric acid in an oven chamber overnight, after which 0.5 mL of H_2O_2 was added. The mixed solutions were heated at 160 °C in a high-pressure reaction container until all samples were completely digested and dried at 120 °C. The Au levels in the tissue samples were quantified by ICP-MS (Agilent 7700, CA, USA).

2.6. BBB in vitro model

To establish an *in vitro* BBB model, transwell polycarbonate inserts (filter pore diameter 3 μm, Corning, USA) were used. HCMEC/D3 cells (BNCC337728, BNCC, Beijing, China) and SVG p12 cells (CRL-8621, ATCC, VA, USA) were separately seeded in the upper and lower chambers, and they were separately cultured for 24 h. Subsequently, the upper chamber was inserted into the lower chamber, and the co-culture was maintained for several days to assess the establishment of barrier integrity. This was achieved by measuring transepithelial electrical resistance (TEER) values using an epithelial volt-ohm meter (Millicell ERS-2, MA, USA). The BBB model achieved a maximum TEER value of 540 ± 7.5 Ω cm^2 after 4 days of culture, confirming the viability of the model for studying BBB integrity changes when

exposed to Au-rGO (Supporting Information Fig. S1). Thus, in the follow-up experiments, Au-rGO was administered on the fourth day after seeding.

2.7. Transwell permeability test

BBB paracellular permeability was assessed using two parameters: TEER values and sodium fluorescein (Na-Flu) permeability. Once BBB integrity was established, Au-rGO was introduced into the upper chamber at various doses and for different exposure durations, with or without MT-regulating agents. TEER values were measured both before and after drug exposure. Changes in TEER data were calculated after standardization with the initial value. Na-Flu is a commonly employed indicator to gauge barrier disruption since it can permeate into the lower chamber through the BBB's paracellular route. Following exposure to Au-rGO, Na-Flu (200 μg/mL in Earle's balanced salt solution) was added to the upper chamber and incubated in the dark for 2 h. Subsequently, 100 μL of Earle's balanced salt solution from the lower chamber was tested to quantify the concentration of Na-Flu *via* its fluorescence intensity using a microplate reader (Molecular Device SpectraMax i3X, CA, USA).

2.8. Western blot (WB) analysis

For protein analysis, brain tissues and HCMEC/D3 cells were lysed and separated by sodium dodecyl sulfate-polyacrylamide gel electrophoresis (SDS-PAGE) using protein electrophoresis and blotting equipment (Bio-Rad, CA, USA). The primary antibodies were used: α-tubulin (Proteintech 11224-1-AP/66031-1-lg, IL, USA), β-tubulin (Proteintech 10094-1-AP, IL, USA), α-catenin (HuaAn Biotechnology ET1610-46, Hangzhou, China), β-catenin (Cell Signaling Technology 8480, MA, USA), VE-cadherin (Santa Cruz Biotechnology sc-9989, TX, USA), ZO-1 (Proteintech 21773-1-AP, IL, USA), claudin-5 (Abcam AB131259, Cambridge, UK), occludin (Proteintech 27260-1-AP, IL, USA), tau (Santa Cruz Biotechnology sc-32274, TX, USA), MAP4 (Proteintech 11229-1-AP, IL, USA), p-GSK3β (HuaAn Biotechnology ET1607-60, Hangzhou, China), GSK3β (HuaAn Biotechnology ET1607-71, Hangzhou, China), crmp2 (HuaAn Biotechnology ER1802-45, Hangzhou, China), acetylated-tubulin (Proteintech 66200-1-lg, IL, USA), p-ERK (Proteintech 28733-1-AP, IL, USA), ERK (Proteintech 11257-1-AP, IL, USA), p-stathmin (Cell Signaling Technology 4191, MA, USA), stathmin (Proteintech 11157-1-AP, IL, USA), p-c-Raf (Cell Signaling Technology 9427, MA, USA), c-Raf (Cell Signaling Technology 9422, MA, USA), p-MEK1/2 (Cell Signaling Technology 9121, MA, USA), MEK1/2 (Cell Signaling Technology 9122, MA, USA) and GAPDH (Proteintech 60004-1-lg/10494-1-AP, IL, USA). The blots were detected using an enhanced chemiluminescence detection system (Tianon 5200, Chengdu, China), and the optical densities of the bands were analyzed using ImageJ analyzer software.

To assess soluble and polymeric tubulins, HCMEC/D3 cells after drug administration were incubated with an MT stabilization buffer according to a previously published formula and protocol[31]. After centrifugation (21,900×g) of the MT stabilization buffer, the supernatant was extracted and designated as soluble tubulins. The remaining fraction containing polymeric tubulin was lysed in RIPA buffer. Immunoblotting was then performed using α-tubulin and β-tubulin antibodies.

2.9. Cell IF staining

HCMEC/D3 cells were fixed, permeabilized, and incubated overnight at 4 °C with primary antibodies, including α-tubulin (Proteintech 66031-1-lg, IL, USA), α-catenin (Proteintech 12831-1-AP, IL, USA), and ZO-1 (Proteintech 21773-1-AP, IL, USA). Nuclei were counterstained with DAPI (Leagene BioBiotechnology DA0800, Huaibei, China), and microfilaments were stained with phalloidin (Thermo Fisher Scientific R415, MA, USA). Images were acquired using a laser scanning confocal microscope (Zeiss LSM980, Oberkochen, Germany).

2.10. Molecular dynamics simulation

Structure modeling: The Au-rGO structure was composed of Au and a rGO planar structure generated from the graphene function of gmxtools. Since Au nanoparticles and rGO sheets are bound by the van der Waals force and do not form ionic or covalent bonds, gold atoms are randomly added to the system and adsorbed on the rGO sheets (Supporting Information Fig. S2). The RDKit was used to call the MMFF94 force field for structural optimization. The protein model of the tubulin dimer was downloaded from the PDB database (id: 1TUB), and the irrelevant inorganic salts and crystal water were removed.

Molecular dynamics: molecular dynamics simulations were performed using the Gromacs 2019.6 program. The initial system was designed to investigate the impact of Au-rGO on a single tubulin dimer, which consisted of an Au-rGO sheet and a single tubulin dimer, all surrounded by TIP3P waters, with Na^+ and Cl^- ions added to neutralize the system. The periodic boundary condition was set with a minimum distance of 10 Å between the complex and the box's edges. To explore the effects of Au-rGO on MTs, two additional systems were created. One only contained laterally paired tubulins, while the other included both laterally paired tubulins and an Au-rGO sheet. The influence of Au-rGO on MTs was assessed by comparing the differences between the laterally paired tubulins in the two systems.

At the start of the molecular dynamics simulations, receptor topology files were generated using the Amber14sb force field for the tubulin dimers and the Sobtop1.0 for Au-rGO. The systems underwent two phases of equilibration, each lasting 1000 ps, at a constant temperature of 300 K and constant pressure. The equilibration phases encompassed constant particle number, volume, and temperature equilibration. After equilibration, molecular dynamics simulations were run for 100 ns, with a time step of 2 fs. Covalent bond lengths were constrained using the Linear Constraint Solver algorithm, and long-range electrostatic interactions were computed using the Particle Mesh Ewald method. Water molecules were treated with the SETTLE algorithm. Trajectories were recorded at 10 ps intervals for subsequent analysis. The non-bonding interaction cutoff was set at 10 Å.

Root mean square deviation (RMSD) was used to observe the local site modification of the system during the simulation (the cut-off point of the fluctuation was set to 0.2). The radius of gyration (RG) was used to evaluate the tightness of the architecture. The solvent-accessible surface area (SASA) was determined to observe the size of the complex during the simulation. The binding free energy was calculated using gmx_MMPBSA. PyMOL 2.5.1 and LigPlot 2.1 are used for visualization.

2.11. TEM observation of cells

HCMEC/D3 cells were exposed to 20 μg/mL Au-rGO for 1 h, followed by extensive washing to remove extracellular Au-rGO.

The cells were collected and fixed in 2.5% glutaraldehyde. After a dehydration process using varying ethanol concentrations, the cells were subsequently embedded in Epon resin. Ultrathin sections measuring 500 nm were prepared on hexagonal mesh grids and examined using a TEM (Hitachi H-7500, Tokyo, Japan).

2.12. Modified protein pull-down assay

To determine the proteins adsorbed onto the materials, we designed a modified protein pull-down assay using Au-rGO based on previously published methods[32,33]. Briefly, HCMECs/D3 cells were exposed to 20 μg/mL Au-rGO for 1 h, after which they were directly lysed, collected, and centrifuged at 1000×*g* for 10 min. The supernatant was removed, leaving the Au-rGO and proteins attaching to them, which we referred to as "sample 1". In parallel, an equivalent number of HCMECs/D3 cells were first lysed, and the resulting cell lysate was then incubated with the same quantity of Au-rGO as in sample 1 for 1 h, labeled as "sample 2". Additionally, the cell lysate was incubated with agarose beads alone, labeled as "sample 3", and agarose beads with either α-tubulin or β-tubulin antibody, labeled as "sample 4". They were incubated at 4 °C for 4 h, following the common protein pull-down assay protocol. Sample 3 served as a negative control, while sample 4 served as a positive control. Subsequently, the cell lysates from the four groups were transferred to spin columns and centrifuged at 1000×*g* at 4 °C for 5 min to separate the supernatant from Au-rGO or beads and their surface-adhered proteins. Each sample underwent five washes with washing buffer to eliminate non-adhered proteins. Finally, the Au-rGO or beads were washed three more times with elution lysis buffer to remove proteins that adhered to their surfaces. The resulting protein lysates were thermally denatured with loading buffer and separated by SDS-PAGE. Protein presence was visualized with Coomassie blue dye, while WB was used to determine the types of proteins adsorbed onto the Au-rGO sheet. Protein quantification was expressed as the integral optical density value.

2.13. Tubulin polymerization assay

The standard assay was conducted in a half-area black 96-well plate with a flat bottom, using a fluorimeter at 37 °C, with observations taken every 30 s for 90 min. The standard initial system consisted of 2 mg/mL tubulin in a buffer containing 80 mmol/L piperazine-1,4-bisethanesulfonic acid at pH 6.9, 2.0 mmol/L $MgCl_2$, 0.5 mmol/L ethylene glycol tetraacetic acid, 1.0 mmol/L guanosine triphosphate, and 15% glycerol. To investigate the effects of Au-rGO on dissociated tubulin, various test compounds, including PBS, Au-rGO (0.1 mg/mL), and Colchicine (Col, 30 μmol/L), were individually introduced into the initial system. To study the impact of Au-rGO on assembled MTs, the initial system was pre-incubated for 30 min to allow stable MT formation before adding the test compound. The experimental procedures followed the manufacturer's protocols (Cytoskeleton Inc Tubulin Polymerization Assay kit, CO, USA).

2.14. TEM observation of purified MTs

MTs in this experiment were polymerized from a system composed of tubulins at a concentration of 4 mg/mL in a buffer with pH 6.8, containing 1.0 mmol/L $MgCl_2$, 1.0 mmol/L EGTA, 1.0 mmol/L GTP, and 5% glycerol. This system was incubated at 37 °C for 20 min. Subsequently, PBS, Au-rGO, and Col were separately introduced into the system and incubated for 1 h at 37 °C. After drug administration, MTs were stabilized by the addition of paclitaxel (Ptx, 20 μmol/L) and observed at room temperature. To facilitate the observation of MTs with TEM, spermine (10 mmol/L) was added to the system to form MT bundles. The samples were observed using a transmission electron microscope (Hitachi H-7650, Tokyo, Japan).

2.15. RNA-seq assay

Total RNA was extracted from HCMEC/D3 cells exposed to either 0 or 20 μg/mL Au-rGO for 2 h using TRIzol reagent (Invitrogen, CA, USA). The RNA samples were assessed for quality, followed by library preparation for transcriptome sequencing using the NEBNext® library preparation kit (NEB, USA). Clustering of the libraries was performed on a cBot Cluster Generation System (using the TruSeq PE Cluster Kit v3-cBot-HS). Differential expression analysis was conducted using the DESeq2 R package (version 1.16.1). DESeq2 was conducted based on the negative binomial distribution to determine differential expression in digital gene expression data, and the resulting *P*-values were adjusted using Benjamini and Hochberg's approach to control the false discovery rate. Genes with an adjusted $P < 0.05$, as determined by DESeq2, were considered differentially expressed. Gene ontology enrichment analysis and Kyoto Encyclopedia of Genes and Genomes pathway analysis of the differentially expressed genes were performed using the clusterProfiler R package.

2.16. Co-immunoprecipitation (Co-IP)

HCMEC/D3 cells were exposed to 20 μg/mL Au-rGO for 2 and 6 h, after which they were lysed using a lysis buffer. Whole-cell lysates were obtained and subsequently incubated with protein A sepharose beads along with the capture antibody targeting stathmin (HuaAn Biotechnology ET1609-20, Hangzhou, China). The immunocomplexes were then precipitated and washed following the manufacturer's instructions (Proteintech KIP-1, IL, USA). The Co-IP protein samples were separated by SDS-PAGE according to the protocols outlined for WB assays.

2.17. Statistical analyses

All results are presented as "Means ± Standard Deviation (SD)" and analyzed using the IBM SPSS Statistics Processor (version 26.0). Normality of the data was assessed using the Kolmogorov−Smirnov test. For data that followed a normal distribution, the statistical significance of differences among multiple groups was evaluated using One-way ANOVA. LSD *post hoc* test was applied when the data exhibited homogeneity of variance, while Dunnett's T3 *post hoc* test was used when the data showed heterogeneity of variance. Non-normally distributed data were analyzed using the Kruskal−Wallis H test, followed by Dunnett's T3 test for *post hoc* analysis. $P < 0.05$ was considered statistically significant.

3. Results and discussions

3.1. Characterization of Au-rGO and its effect on BBB opening

GO was synthesized using the Hummers' method, and the Au-rGO was prepared by a simultaneous reduction technique[34], using

glucose as a reducing agent under alkaline conditions. Oxygen-containing functional groups on the GO surface promote the adsorption of free metal ions *via* electrostatic interactions, which is followed by the reduction of the metal ions using a reducing agent and the subsequent growth of AuNPs on the rGO sheets[35]. SEM and TEM analysis revealed the distribution of AuNPs on the surface of the graphene sheet (Fig. 1A and B). Raman spectral characterization demonstrated the presence of key features in the Au-rGO material, notably a pronounced D peak at 1345 cm^{-1} and a characteristic G peak at 1604 cm^{-1}, which signify the existence of graphitic sp^2 carbon regions and hybrid structural defects arising from oxygen-containing functional groups and edges within the Au-rGO sheets (Fig. 1C). The Fourier transform infrared spectrum demonstrated that peaks associated with oxygen functional groups were substantially diminished in Au-rGO (Fig. 1D). TEM imaging revealed an interplanar spacing of 0.197 nm, which is consistent with the (200) crystal plane of gold, indicating that the synthesized particles are crystalline gold (Fig. 1E). The size distribution showed that most of the AuNPs were dispersed in the range of 15−25 nm (Fig. 1F). X-ray diffraction analysis displayed distinctive peaks for gold, and the estimated size of the AuNPs from the peak width of the (111) (200) (220) (311) (222) Bragg reflection was approximately 21.1 nm, using the Scherrer formula (Fig. 1G), which is consistent with the previous results. Atomic force microscopy results depicted Au-rGO as a single-layer nanosheet with a height of approximately 25 nm, and a size of roughly 150 nm (Fig. 1H). However, Au-rGO nanosheets exhibited agglomeration when suspended in PBS and culture medium (Fig. 1I). The gold content in Au-rGO was quantified using ICP-OES, which showed a gold weight percentage of approximately 3.8%. To evaluate the stability of the AuNP modification, Au-rGO was dispersed and sonicated in PBS, freeze-dried, and then reanalyzed by ICP-OES. The results indicated no significant difference in gold content before and after PBS treatment (Fig. 1J). Furthermore, SEM combined with energy dispersive spectrometer mapping confirmed that the AuNPs remained uniformly distributed on the graphene surface following PBS dispersion (Fig. 1K), demonstrating that

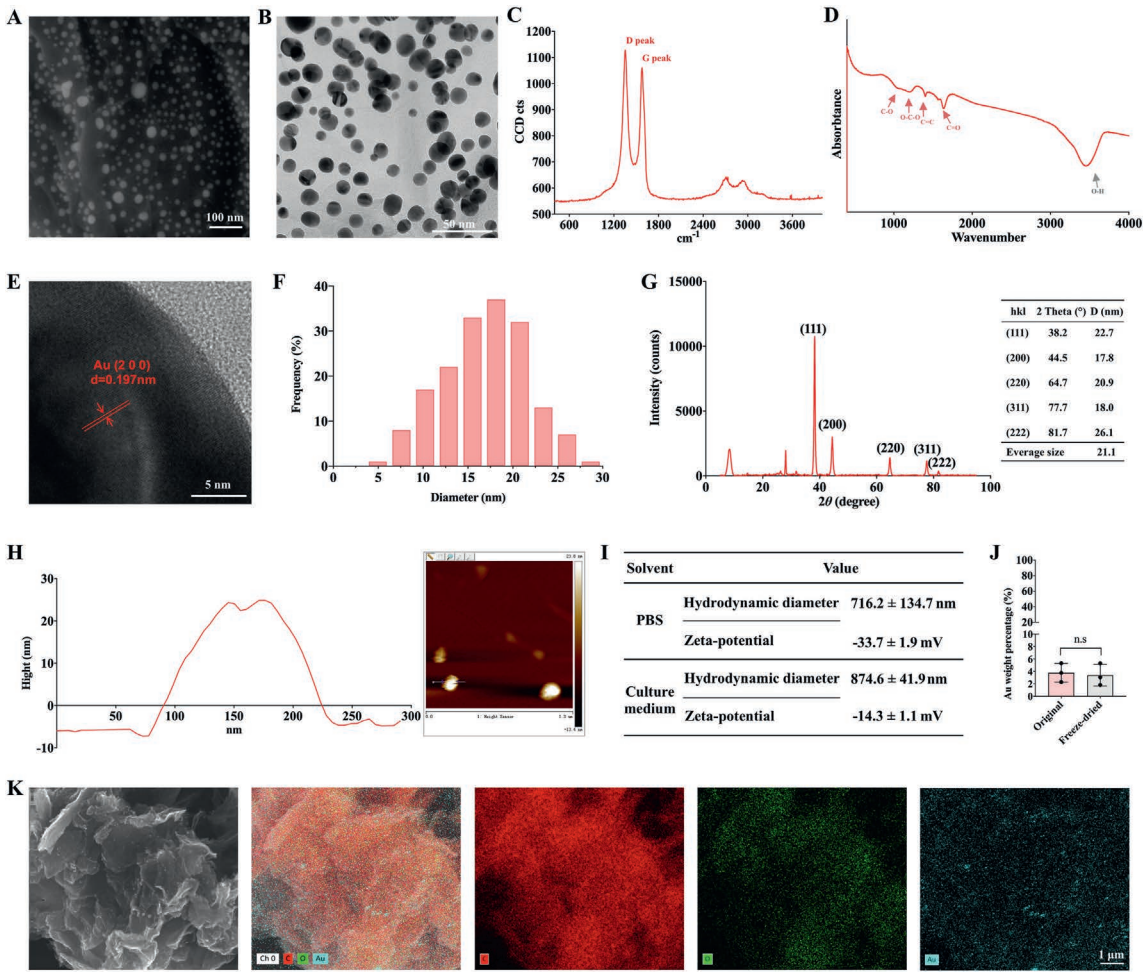

Figure 1 Characterization of gold nanoparticle-modified reduced graphene oxide (Au-rGO). (A) Scanning electron microscope (SEM) image of Au-rGO. (B) Transmission electron microscope (TEM) image of Au-rGO. (C) Raman spectrum of Au-rGO. D peak: 1345 cm^{-1}; G peak: 1604 cm^{-1}. (D) Fourier transform infrared spectrum of Au-rGO. (E) Interplanar spacing of AuNPs. (F) Size distribution of gold nanoparticles (AuNPs). (G) X-ray diffraction pattern of Au-rGO. (H) Atomic force microscopy image of Au-rGO showing the topography and height profile. (I) Hydrodynamic diameter and zeta-potential of Au-rGO in PBS and culture medium. (J) Gold weight percentage of original Au-rGO and freeze-dried Au-rGO. Data are represented as the mean ± SD ($n = 3$). (K) Elemental composition of Au-rGO detected by energy dispersive spectrometer mapping.

the AuNPs did not readily detach from the rGO sheets. Together, these results confirm the successful attachment of AuNPs to the rGO sheets and provide a thorough characterization of the physicochemical properties of Au-rGO.

Here, we first investigated the BBB opening efficacy of Au-rGO through *in vivo* experiments. Before animal experimentation, the hemolysis rates of Au-rGO and related components were evaluated and were found to be below 1% in all cases, indicating excellent hemocompatibility and supporting their suitability for intravenous administration (Supporting Information Fig. S3). Different doses of Au-rGO were intravenously administered to C57BL/6 mice, and after a 2-h post-injection period, we evaluated BBB permeability using the Evans blue permeability test, as illustrated in Fig. 2A. This time point was selected based on the typical duration required for most previously studied nanomaterials to traverse the BBB following intravenous injection[36]. The results revealed varying degrees of blue staining in brain tissues, which demonstrates the effectiveness of Au-rGO in opening the BBB (Fig. 2B). However, it is essential to recognize that for BBB drug delivery, only opening the BBB is insufficient, as the BBB should also rapidly reclose and regain its integrity to ensure treatment and patient safety[37]. Therefore, we monitored changes in BBB integrity at different time intervals following administration of Au-rGO at a dose of 4 mg/kg body weight and found that the intensity of staining in the brain tissues increased for the first 2 h and then gradually diminished (Fig. 2C). The observed changes in staining patterns provide compelling evidence of the BBB opening dynamics, indicating that BBB opening

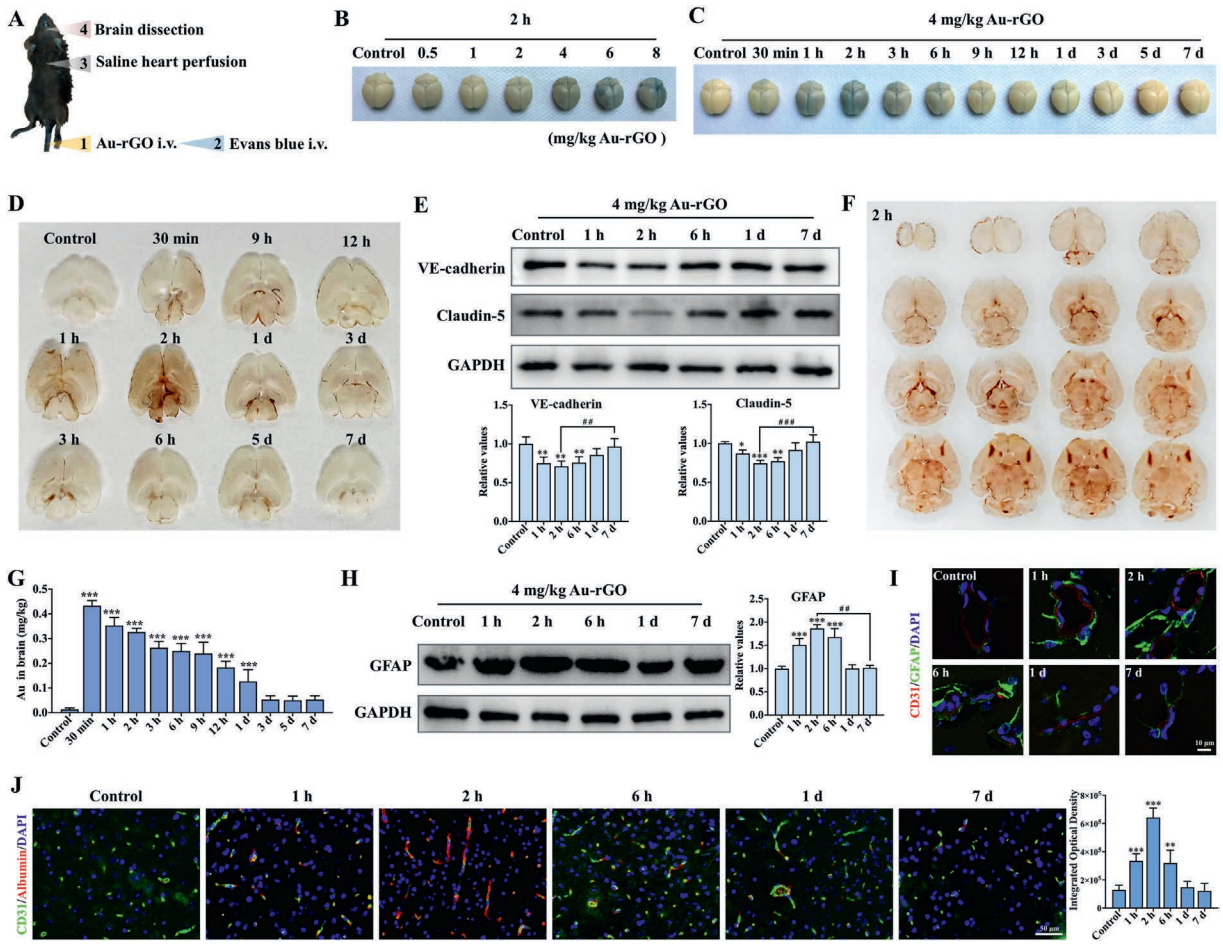

Figure 2 The BBB-reversible opening effects by Au-rGO *in vivo*. (A) Schematic representation of Au-rGO exposure and the Evans blue permeability test *in vivo*. (B) Brain tissue staining with Evans blue from mice intravenously exposed to Au-rGO at different doses. (C) Brain tissue staining with Evans blue from mice intravenously exposed to Au-rGO at a dose of 4 mg/kg body weight for various durations ($n = 3$). (D) Vibratome sections of brain tissue stained with horseradish peroxidase from mice exposed to Au-rGO at a dose of 4 mg/kg body weight for different time points ranging from 30 min to 7 days. (E) Immunoblot analysis of VE-cadherin and Claudin-5 in brain tissue from mice exposed to Au-rGO at a dose of 4 mg/kg body weight for 1, 2, 6 h, 1 day, and 7 days. (F) Top-to-bottom continuous brain sections from mice exposed to Au-rGO at a dose of 4 mg/kg body weight for 2 h. (G) Measurement of Au content as an indicator of Au-rGO retention in brain tissue using the inductively coupled plasma mass spectrometry (ICP-MS). (H) Immunoblot analysis of glial fibrillary acidic protein (GFAP) in brain tissue from mice exposed to Au-rGO at a dose of 4 mg/kg body weight for 1, 2, 6 h, 1 day, and 7 days. (I) IF staining of GFAP (green) reveals reactive astrocytes around brain vessels, with CD31 (red) used to mark brain vessels. Scale bar: 10 μm. (J) IF staining of albumin (red) extravasation around brain vessels, with CD31 (green) used to mark brain vessels. Scale bar: 50 μm. Data are represented as the mean ± SD ($n = 5$ for the rest of the *in vivo* experiments). $^{*}P < 0.05$, $^{**}P < 0.01$, and $^{***}P < 0.001$ compared with the control group. $^{\#}P < 0.05$, $^{\#\#}P < 0.01$ and $^{\#\#\#}P < 0.001$ compared between the two experiment groups.

started as early as 30 min after the administration of Au-rGO, with the most significant BBB opening occurring at the 2-h mark, followed by a gradual recovery of barrier integrity. To further validate these findings, we employed additional experimental methods to assess the status of BBB opening and closure. We used horseradish peroxidase as a tracer to examine BBB leakage, as it reacts with DAB to form a brown product that is easily observable, providing detailed morphological evidence of BBB opening[38]. The presence of dark brown staining in the vibratome sections of brain tissues shows the same trend (Fig. 2D). Besides, we selected brain tissue at representative time points for the detection of two crucial intercellular junction proteins governing the paracellular route of the BBB. WB analysis revealed a significant decrease in these junction proteins at 1, 2, and 6 h, followed by a recovery at 1 and 7 days (Fig. 2E). Collectively, results from all three experiments—from macroscopic structural observations to protein-level analyses—indicate that Au-rGO rapidly reaches the brain following intravenous administration, opens the BBB within 2 h, and fully restores barrier integrity within 24 h.

After determining the effectiveness of the Au-rGO, we also evaluated the safety of the material. Upon examination of brain slices from top to bottom, we observed that the brown DAB reaction products were mainly concentrated around the ventricles and in the cerebral cortex, where Au-rGO primarily exerts its effects (Fig. 2F). Given the presence of AuNPs, we used ICP-MS to determine the retention time of Au-rGO in the brain, which revealed significant material retention in the brain within the first day after administration, but after 3 days, its content notably decreased, with no significant difference compared to the control group (Fig. 2G). WB results and IF images of GFAP suggest that Au-rGO opens the BBB and transiently affects neuroglial cells in the vicinity of the leaking vessels (Fig. 2H and I). However, widespread and prolonged glial activation was not observed, indicating a localized and reversible response stimulated by Au-rGO[39]. Extravasation of blood-derived albumin serves as another key indicator of BBB disruption. IF results revealed that during the period of Au-rGO-induced BBB opening (from 1 to 6 h post-injection), only minimal albumin extravasation was detected around the capillaries. By 1 day after exposure, the extravasated albumin had been largely cleared (Fig. 2J), indicating that the BBB opening was transient and reversible, with no irreversible effects on brain tissue.

Furthermore, H&E staining of the cortex and hippocampus revealed no significant pathological changes at any time point (Supporting Information Fig. S4A). None of the mice from any group exhibited stress or abnormal symptoms, such as lethargy, anorexia, or weight loss, throughout the entire experimental period (Fig. S4B). The levels of Au-rGO in key metabolic organs, the liver and kidney, gradually decreased over time until they were cleared, without causing long-term accumulation (Fig. S4C and S4D). Pathological sections of the liver and kidney did not reveal any abnormalities (Fig. S4E). No symptoms indicative of pulmonary embolism was observed post-injection, and H&E staining of lung tissue revealed no significant lesions (Fig. S4F). To observe long-term effects of Au-rGO and related components, we employed two types of animal model to provide more safety data of AuNPs, rGO and Au-rGO: (1) After a single intravenous injection, the animals were observed for one month, during which the state of the animals was observed, and the tissues of important organs were collected for H&E staining; (2) The animals were injected intravenously once a week for four consecutive times. The state of the animals was observed, and the vital organs were collected for H&E staining one week after the last injection. The results showed that none of the mice from any group exhibited stress or abnormal symptoms, such as lethargy, anorexia, or weight loss, throughout the entire experimental period (Supporting Information Fig. S5A and S5B), and the pathological sections of the brain, liver, kidney, and lung tissues did not reveal any abnormalities (Fig. S5C and S5D). These results collectively indicate that intravenous injection of 4 mg/kg of Au-rGO is relatively safe, and no long-term material retention or damage to the brain or other organs was observed, which highlights the ability of Au-rGO to safely and reversibly open the BBB.

3.2. *Au-rGO reversibly and safely opens the BBB in vitro*

The reversible opening of the BBB by Au-rGO was also verified *in vitro*. We opted for a non-contact co-culture system comprising the human cerebral microvascular endothelial cell line HCMEC/D3 and the human glial cell line SVG p12 to mimic the BBB, and the barrier integrity was mainly measured using TEER value and Na-Flu permeability test (Fig. 3A). In this model, Au-rGO was directly exposed to HCMEC/D3 cells, while SVG p12 cells provided an environment conducive to maintaining BBB stability.

Our initial objective was to determine whether the *in vitro* model could replicate the *in vivo* findings regarding the reversible opening of the BBB by Au-rGO. In our *in vivo* experiments, BBB opening occurred within 2 h after Au-rGO application, with BBB integrity beginning to recover at 6 h. Therefore, for the *in vitro* experiments, we focused our observations within a 6-h timeframe. Cell viability assessments using CCK-8 tests revealed that Au-rGO did not induce significant cell death within the dose range of 0−50 μg/mL (Fig. S6). Subsequently, we identified the appropriate Au-rGO concentration capable of opening the BBB *in vitro* by measuring TEER value, performing a Na-Flu permeability test, and assessing changes in junction protein levels. Given that Au-rGO interacts directly with endothelial cells in the *in vitro* model, the optimal exposure time tends to be earlier than *in vivo* experiments. Therefore, we assessed all experimental indices at 1 h after Au-rGO exposure and observed that exposure to Au-rGO at a dose of 20 μg/mL resulted in a significant decrease in TEER value (Fig. 3B), an increase in Na-Flu permeability (Fig. 3C), and a decrease in the protein levels of VE-cadherin and claudin-5 (Fig. 3D). These results suggest that 20 μg/mL is the effective dose to open the BBB in the *in vitro* experimental models.

Next, we examined the changes in BBB integrity over time when exposed to 20 μg/mL Au-rGO. At 30 min, the TEER value began to decline, but the difference was not statistically significant. However, at 1 h, the TEER value decreased significantly and was lower than that of the control. By 2 h, the TEER began to recover but remained significantly lower than the initial level. Subsequently, the TEER continued to increase, reaching a level significantly higher than the lowest TEER observed at 1 h, and without a significant difference compared to the control level at 6 h (Fig. 3E). The Na-Flu permeability test showed a similar pattern (Fig. 3F). At the molecular level, both AJ proteins (α-catenin, β-catenin, and VE-cadherin) and TJ proteins (ZO-1, claudin-5, and occludin), which are located on the cell membrane and regulate BBB paracellular permeability, exhibited significant changes. Although the extent of change for each protein varied at each time point, all proteins showed a significant decline at 1 h, and a significant increase at 6 h compared to the lowest levels observed (Fig. 3G and H). These findings collectively provide

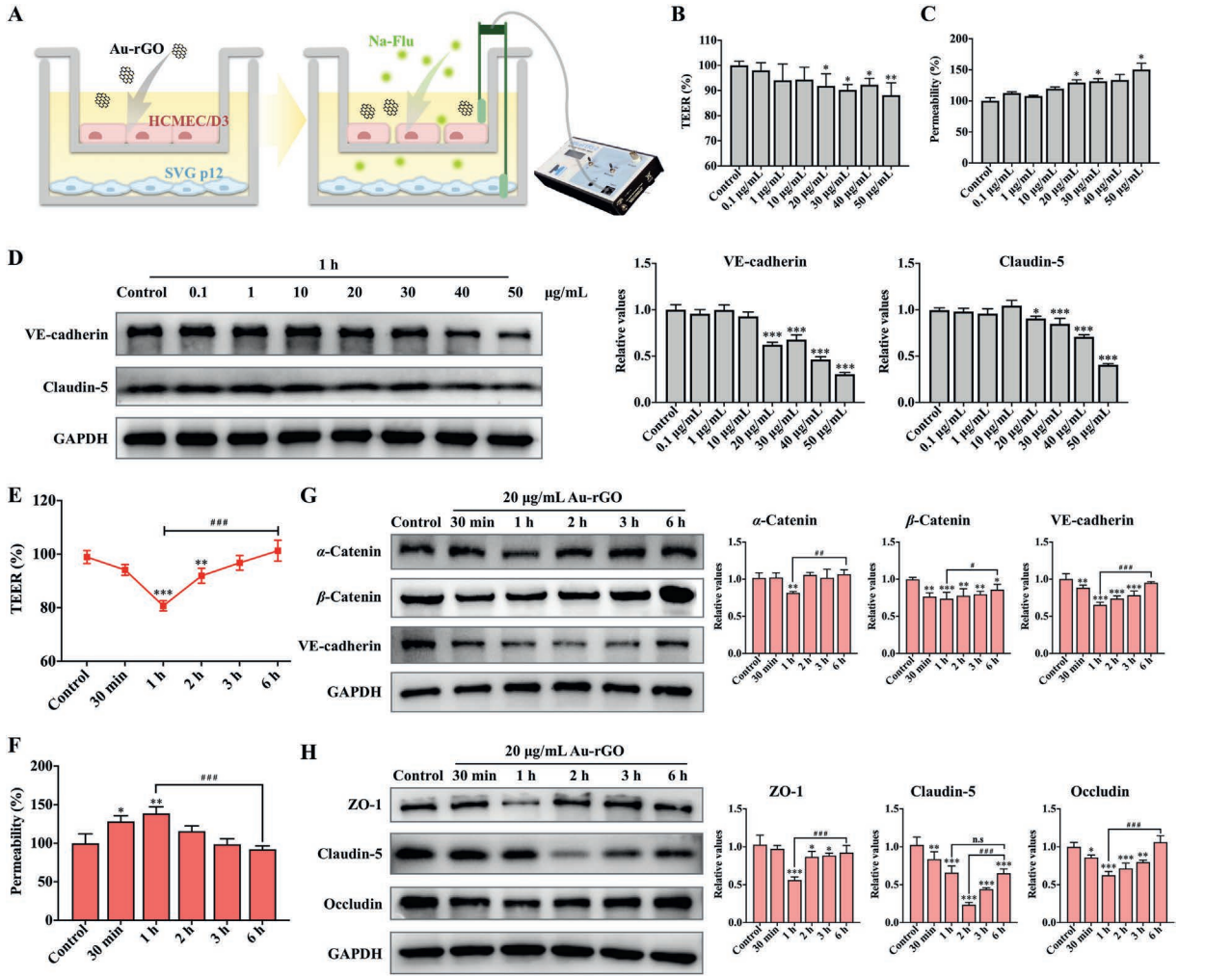

Figure 3 Au-rGO reversibly opens the BBB *in vitro*. (A) Schematic representation of the *in vitro* BBB experimental model. (B) Transepithelial electrical resistance (TEER) value of the BBB exposed to Au-rGO at doses of 0.1, 1, 10, 20, 30, 40, and 50 μg/mL for 1 h. (C) Sodium fluorescein (Na-Flu) permeability of the BBB exposed to Au-rGO at doses of 0.1, 1, 10, 20, 30, 40, and 50 μg/mL for 1 h. (D) Immunoblot analysis of VE-cadherin and claudin-5 of HCMEC/D3 cells exposed to Au-rGO at doses of 0.1, 1, 10, 20, 30, 40, and 50 μg/mL for 1 h. (E) TEER values of the BBB exposed to 20 μg/mL Au-rGO for various durations (30 min, 1, 2, 3, and 6 h). (F) Na-Flu permeability of the BBB exposed to 20 μg/mL Au-rGO for various durations. (G) Immunoblot analysis of adherens junctions (AJs) components, including α-catenin, β-catenin, and VE-cadherin on the cell membrane of HCMEC/D3 cells exposed to 20 μg/mL Au-rGO for various durations. (H) Immunoblot analysis of tight junctions (TJs) components, including ZO-1, claudin-5, and occludin on the cell membrane of HCMEC/D3 cells exposed to 20 μg/mL Au-rGO for various durations. Data are represented as the mean ± SD ($n = 3$). $^{*}P < 0.05$, $^{**}P < 0.01$, and $^{***}P < 0.001$ compared with the control group. $^{\#}P < 0.05$, $^{\#\#}P < 0.01$ and $^{\#\#\#}P < 0.001$ compared between the two experiment groups.

evidence that Au-rGO induces the reversible opening of the BBB paracellular route *in vitro*.

To further demonstrate that the BBB-opening effect of Au-rGO is primarily mediated by the rGO component rather than the AuNPs, we compared the efficacy of Au-rGO with that of rGO alone and AuNPs (20 nm) at equivalent concentrations in both *in vivo* and *in vitro* models. In the *in vivo* BBB permeability assay, brain tissues from mice treated with rGO alone exhibited Evans blue extravasation of varying intensity. The staining intensity increased within the first 2 h and subsequently decreased, indicating that rGO itself can induce reversible BBB opening, similar to Au-rGO (Supporting Information Fig. S7A). Correspondingly, *in vitro* experiments showed that rGO exposure led to a significant reduction in TEER within 1 h post-exposure, followed by a return to baseline levels (Fig. S7B). A significant increase in Na-Flu permeability (Fig. S7C) and a decrease in the expression levels of the junctional proteins VE-cadherin and claudin-5 were observed in the rGO and Au-rGO groups at 1 h (Fig. S7D). In contrast, AuNPs did not elicit significant BBB opening in either model. These results collectively indicate that the BBB-opening effect is mainly attributable to the rGO component, with no substantial contribution from the AuNPs.

3.3. Au-rGO opens the BBB by modulating MT depolymerization

While we have demonstrated the reversible opening of the BBB by Au-rGO, the underlying mechanisms of this process remain unclear. Most previous studies exploring the opening of the BBB induced by nanomedicine have focused on the expression and post-translational

modification of AJ and TJ proteins[18]. Typically, these changes are specific to individual proteins or concentrated within either the TJ or AJ protein classes. However, in our current study, we observed changes in both AJ and TJ proteins, which exhibited a consistent pattern, suggesting that the cytoskeletal structure responsible for anchoring the junction complexes to the cell membrane might be altered. Among the cytoskeletal systems, microfilaments have been widely studied in relation to intercellular junctions[40,41], particularly as key mediators of nanomaterial-induced barrier permeability regulation[42,43]. Given this, we labeled microfilaments with phalloidin and observed that the morphology and distribution of microfilaments remained largely unchanged at different time points (Supporting Information Fig. S8A). Furthermore, we investigated changes in reactive oxygen species (ROS), which are closely related to microfilament-mediated cell permeability alterations[44], and found that cellular ROS levels remained unchanged (Fig. S8B). Therefore, the hypothesis implicating microfilaments as an intermediate mechanism can be ruled out.

In recent years, MTs, another essential component of the cytoskeletal system, have been implicated in influencing biological barrier permeability[18]. Prior research has shown that even minimal disruption of peripheral MTs, while the actin filament system remains intact and no morphological changes are evident, can disturb paracellular permeability[45]. Given the lack of significant changes in microfilaments, we explored whether alterations in MT structure occurred. The IF results revealed a "first depolymerization, then polymerization" change in MT morphology over time following Au-rGO exposure (Fig. 4A). MT depolymerization status based on the ratio of soluble and polymerized tubulin showed that both subunits, α-tubulin and β-tubulin, exhibited a significant increase in their ratios at 30 min, reaching their highest values at 1 h and returning to normal or even lower levels at 6 h (Fig. 4B). WB results aligned with the observations from the IF images, indicating that MT depolymerization was most pronounced when BBB opening was most evident, and MTs exhibited clear polymerization when BBB integrity was restored. The dynamic stability of MTs, characterized by transitions between polymerization and depolymerization, plays a vital role in regulating TJ and AJ permeability[46,47]. Various NPs have been demonstrated to influence MT dynamics in two directions, both of which result in the opening of the paracellular barrier[48-50]. Thus, our findings strongly suggest that MTs may play a pivotal role in mediating the reversible BBB opening induced by Au-rGO.

To establish whether MTs directly regulate the opening of the BBB induced by Au-rGO, we determined the key 1-h time point, which corresponds to the most significant BBB opening by Au-rGO. Col (1 μmol/L), an MT depolymerization agent, served as a positive control, while Ptx (1 nmol/L), a stabilizer of the MT system, was used to mitigate Au-rGO-induced MT depolymerization. We assessed the MT status by measuring the proportion of soluble and polymerized tubulins and found a significant increase in the ratio of soluble to polymerized tubulins in the Au-rGO group, with Ptx effectively reversing the increase induced by Au-rGO (Fig. 4C). Concurrently, we observed that Au-rGO exposure for 1 h significantly decreased the TEER value of the BBB and increased the passage of Na-Flu, which could be reversed by the addition of Ptx, known to reduce Au-rGO-induced MT depolymerization (Fig. 4D and E). We also assessed the levels of AJ and TJ proteins located on the cell membrane, which showed that exposure to both Au-rGO and Col resulted in varying degrees of decrease in junction protein levels. After stabilizing MTs with Ptx, the restoration of junction protein levels on the membrane was observed (Fig. 4F and G). We further examined the distribution of two key proteins, α-catenin of AJ and ZO-1 of TJ, on the cell membrane and their relationship with MTs. Normally, polymerized tubulin bundles make contact with the cell membrane in an approximately vertical orientation, with their ends showing point-like colocalization with junction proteins (Fig. 4H and I: (a) white arrows). Exposure to Au-rGO led to a significant reduction in the fluorescence intensity of junction proteins, the disappearance of the MT bundle, and the loss of colocalization with MTs (Fig. 4H and I: (b)). The addition of Ptx restored the MT bundles, junction proteins, and their colocalization (Fig. 4H and I: (d) white arrows). These results confirmed that Au-rGO depolymerizes MT bundles, preventing MTs from stabilizing the junction complex on the cell membrane, ultimately resulting in BBB opening.

Notably, we also observed a slight difference in the MT changes induced by Au-rGO and Col. Au-rGO led to uniform blurring of tubulin staining. In contrast, Col induced partial spot-like highlighting of MTs (Fig. 4H and I: (c) red arrows), suggesting that MT depolymerization induced by Col involves the substantial breakage of MT bundles. At the same time, Au-rGO likely disrupts the dynamic equilibrium of MT polymerization/depolymerization without directly destroying tubulin bundles. Next, we verify this phenomenon and clarify how Au-rGO precisely affects the MT system.

3.4. Molecular dynamics simulations reveal the interference of Au-rGO on tubulin dimer and MTs

To understand how Au-rGO influences the dynamic equilibrium of MT depolymerization, we investigated typical MT-associated proteins, including Tau and MAP4, which play roles in MT assembly and stability[51], but observed no significant changes in the groups exposed to Au-rGO (Supporting Information Fig. S9A). We also examined classical signaling pathways that regulate MT depolymerization, such as the GSK-3β−Crmp2 pathway[52], but did not observe significant activation in response to Au-rGO (Fig. S9B). Additionally, MT acetylation, which has been reported to interfere with MT polymerization[53], showed no significant changes upon exposure to Au-rGO (Fig. S9C). Based on these results, we ruled out most of the potential molecular mechanisms that could affect the dynamic equilibrium of MT depolymerization/polymerization, leading us to consider the possibility that Au-rGO may directly interact with MTs to disrupt their dynamic equilibrium, as previous studies indicated that GBMs can enter cells and directly interact with various organelles[29]. To explore this possibility further, we intend to conduct molecular dynamics simulations.

Real-time observations and analyses of dynamic and thermodynamic properties of nanomaterials are often challenging using conventional experimental methods. In recent years, molecular dynamics simulations have emerged as a cost−effective and convenient approach to investigate the interactions between nanomaterials and biological macromolecules[54]. To investigate the interaction between dissociated tubulins and Au-rGO, we constructed a molecular dynamic system comprising a single tubulin dimer and an Au-rGO sheet (Fig. 5A). The RMSD reached saturation after approximately 20 ns, indicating the equilibration and reliability of the simulation (Supporting Information Fig. S10A). Throughout the simulation, the total energy of the system exhibited minimal changes, indicating its stability (Fig. S10B). Over the 100 ns equilibration period, there was a noticeable decrease in the distance between the tubulin centroid

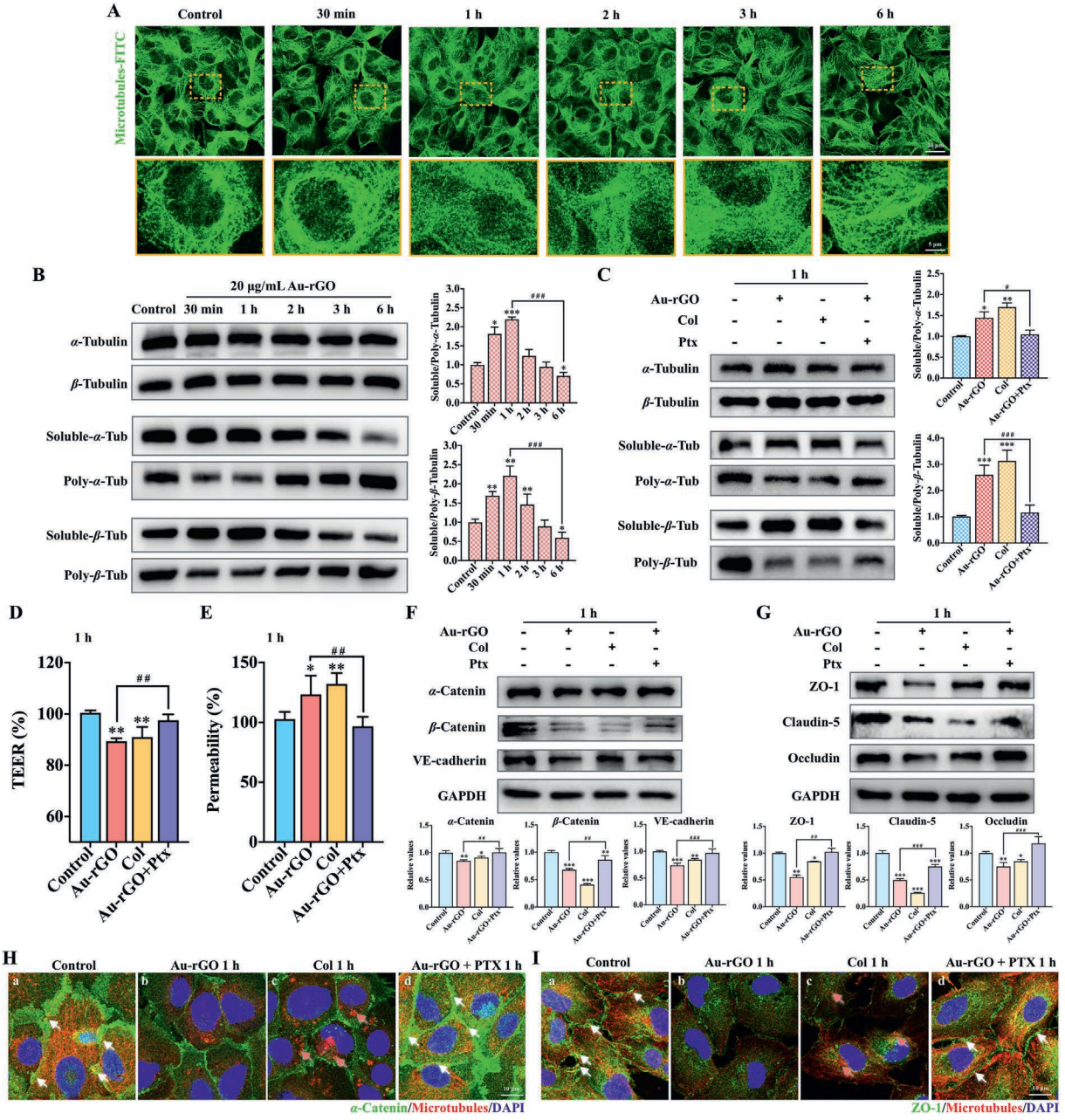

Figure 4 Au-rGO opens BBB by inducing MT depolymerization. (A) IF staining of MTs using α-tubulin antibody in HCMEC/D3 cells exposed to 20 μg/mL Au-rGO for 30 min, 1, 2, 3, and 6 h. The first panel shows microtubules (MTs) under low power, while the second panel provides an enlargement of the boxed area in the first panel. Scale bar: 20 μm in main images; 5 μm in zoomed images. (B) Immunoblot analysis of total, soluble, and polymerized α-tubulin and β-tubulin in HCMEC/D3 cells exposed to 20 μg/mL Au-rGO for varying durations. (C) HCMEC/D3 cells were exposed to a culture medium as the control group, Au-rGO (20 μg/mL) as the experimental group to induce MT depolymerization, colchicine (Col) as a positive control to induce MT depolymerization, and paclitaxel (Ptx) to rescue Au-rGO-induced MT depolymerization, all for a duration of 1 h. Immunoblot analysis of total, soluble, and polymerized α-tubulin and β-tubulin in various samples. (D) TEER values of different samples. (E) Na-Flu permeability results for different samples. (F, G) Immunoblot analysis of AJ and TJ proteins in different samples. (H, I) Immunostaining of HCMEC/D3 cells for α-catenin (H) and ZO-1 (I) (green), MTs (red), and cell nuclei (blue). Scale bar: 10 μm. Point-like colocalization of MTs with junction proteins is indicated by white arrows, while spot-like highlighted MTs are indicated by red arrows. Data are represented as the mean ± SD ($n = 3$). $^{*}P < 0.05$, $^{**}P < 0.01$, and $^{***}P < 0.001$ compared with the control group. $^{\#}P < 0.05$, $^{\#\#}P < 0.01$ and $^{\#\#\#}P < 0.001$ compared between the two experiment groups.

and the Au-rGO sheet centroid (Fig. 5B). Binding free energy calculations revealed a total binding energy of −117.24 kcal/mol between the tubulin dimer and the Au-rGO sheet (Fig. S10C), confirming strong binding between the protein and the material, consistent with the attractive proximity observed in Fig. 5B. The snapshots of the simulation system at various time points also revealed that the Au-rGO sheet exhibited a certain adsorption effect on the single tubulin dimer (Fig. 5C).

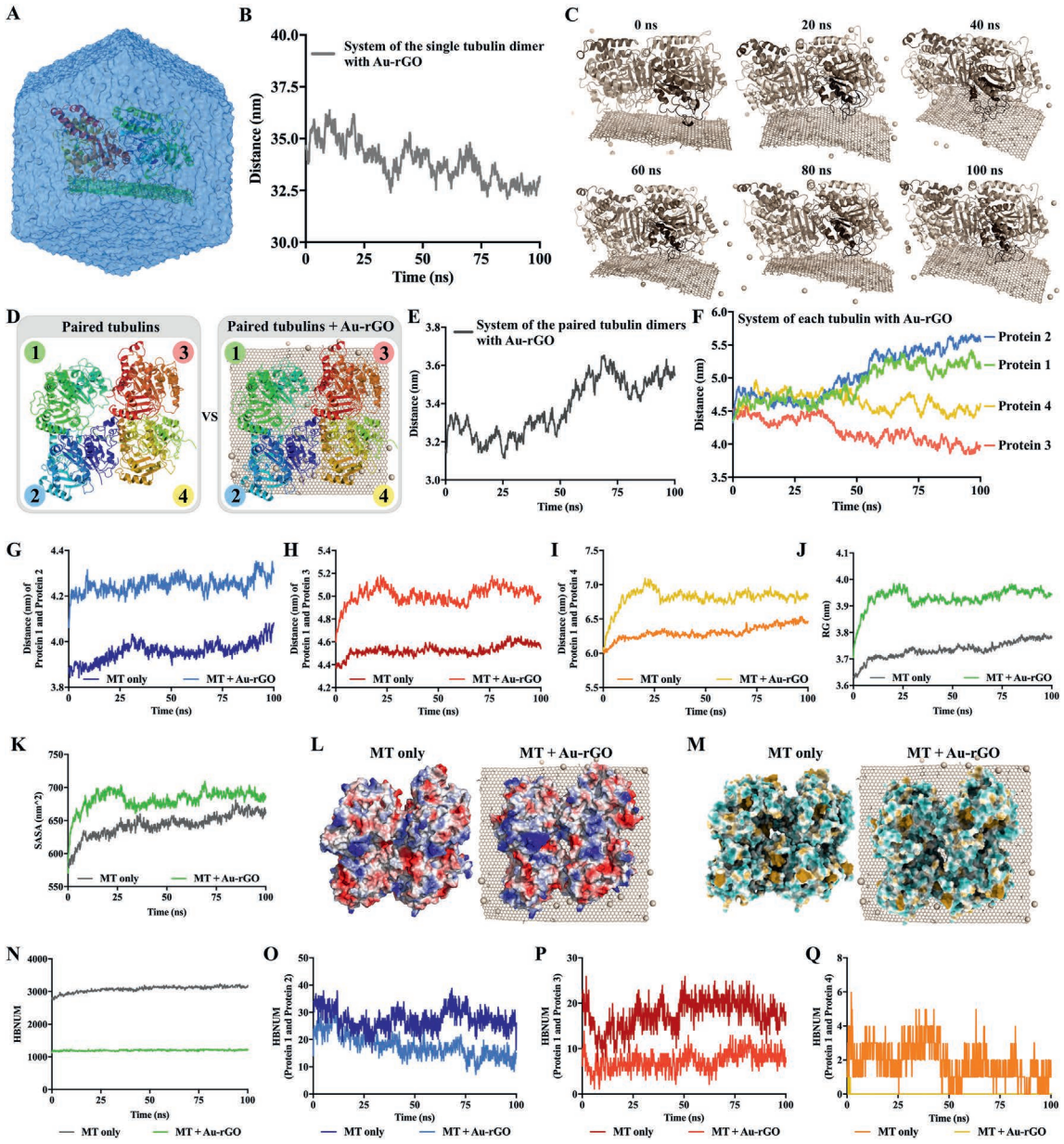

Figure 5 Molecular dynamics simulations of Au-rGO interference on tubulin dimer and MTs. (A) The initial structure of the system consisted of an Au-rGO sheet and a single tubulin dimer placed in a dodecahedral aqueous solution box. (B) The distance between the centroid of the single tubulin dimer and the centroid of the Au-rGO sheet. (C) Snapshots of the single tubulin dimer and Au-rGO sheet system from the simulation trajectory. (D) Front view of the simulation system of laterally paired tubulins without and with Au-rGO tubulins. (E) The distance between the centroid of the laterally paired tubulins and the centroid of the Au-rGO sheet. (F) The distance between each tubulin protein of the laterally paired tubulins and the Au-rGO sheet. (G—I) Distances between Protein 1 and Protein 2/3/4 in the two systems. (J) Radius of gyration of the laterally paired tubulins in the two systems. (K) Solvent-accessible surface area of the laterally paired tubulins in the two systems. (L) Molecular electrostatic potential distribution of the laterally paired tubulins without and with the Au-rGO sheet (regions of negative potential in red and regions of positive potential in blue). (M) Hydrophobic surface distribution of the laterally paired tubulins without and with the Au-rGO sheet (hydrophilic regions in green and lipophilic regions in yellow). (N) Total hydrogen bonding number of the laterally paired tubulins in the two systems. (O—Q) Total hydrogen bonding number between Protein 1 and Protein 2/3/4 in the two systems.

To investigate the impact of Au-rGO on MTs, we constructed two systems: one comprised laterally paired tubulins only (serving as a simplified model of MTs), and the other included laterally paired tubulins with an added Au-rGO sheet (Fig. 5D). Apart from the presence or absence of the Au-rGO sheet, all initial conditions and simulation parameters for both systems were identical. When investigating the interaction between dissociated tubulin dimers and Au-rGO, we considered the tubulin dimer as an independent protein molecule. Our focus was on the adsorption effect of Au-rGO on the tubulin dimer rather than conformational changes within the protein itself; therefore, a single simulation system was deemed sufficient. In contrast, when studying the effect of Au-

rGO on MTs—which are composed of multiple protein subunits—the dynamics simulation inherently involves greater complexity. Structural fluctuations may occur even in the absence of external nanomaterials. Thus, to ensure that observed changes were indeed attributable to Au-rGO and not to intrinsic dynamics, we included a control system containing only tubulin dimers without Au-rGO for comparison.

RMSD values for both systems reached saturation after approximately 20 ns, indicating equilibration and the reliability of the simulations (Fig. S10D and S10E). For a 100 ns equilibration period, the distance between the centroid of the laterally paired tubulins and the Au-rGO sheet slightly increased (Fig. 5E), indicating an interaction pattern distinct from that observed between the single tubulin dimer and the Au-rGO sheet. Thus, we examined the distances between four tubulin proteins and the Au-rGO sheet separately. Notably, the distances between Protein 1 and 2 and the Au-rGO sheet significantly increased, while the distances between Protein 3 and 4 and the Au-rGO sheet slightly decreased (Fig. 5F). These findings indicate that the four subunits display inconsistent movements relative to the Au-rGO sheet. Subsequently, we calculated the distances between Protein 1 and Protein 2, 3, and 4 in both systems and compared the data, which revealed that the distance between the four tubulin proteins in the system with Au-rGO was significantly greater than in the natural state without Au-rGO (Fig. 5G—I). These findings suggest that the four tubulin proteins experienced different interaction forces exerted by the Au-rGO sheet, causing them to separate from each other, either between the upper and lower subunits of the same dimer or between neighboring dimers. We also calculated two additional parameters: the RG, reflecting the tightness of the protein structure, and the SASA, indicating the surface area of a biomolecule accessible to a solvent. The results showed that both RG and SASA values were greater in the system with the Au-rGO sheet (Fig. 5J and K), indicating that the Au-rGO sheet caused the laterally paired tubulins to stretch and become less consolidated, further supporting the previous observations. It has been reported that a graphene nanosheet can separate one dimer from another through a "tug-of-war" mechanism when placed vertically near the dimer—dimer interface[55]. However, in actual scenarios, the graphene sheet might also contact the MTs horizontally. Therefore, in this study, we initially placed the Au-rGO sheet parallel to MTs, providing a complementary perspective to previously reported models. Regardless of the initial placement direction, the graphene sheet caused MTs to loosen, and tubulin dimers moved away from each other.

The exact reasons for the loosening of the laterally paired tubulins are complex. We compared the molecular electrostatic potential and the hydrophobic surface of the laterally paired tubulins with and without the Au-rGO sheet and found that these properties exhibited irregular changes (Fig. 5L and M). Then, we calculated the hydrogen bonding number for the entire system (Fig. 5N) and between each protein (Fig. 5O—Q). The results indicated that Au-rGO significantly reduced the hydrogen bonding number for the entire system and between different tubulin proteins. It is well-established that the formation and number of hydrogen bonds influence the conformation of protein molecules. Previous reports suggested that fullerene derivatives could inhibit MT polymerization by forming hydrogen bonds with proteins[49]. However, a more detailed and comprehensive analysis of the molecular dynamics in this tubulin—Au-rGO system is needed for a complete understanding.

3.5. Au-rGO can adsorb dissociated tubulin dimers and induce assembled MTs to depolymerize

The molecular dynamics simulation results suggest that Au-rGO can adsorb dissociated tubulin dimers and induce assembled MTs to depolymerize, thereby interfering with the dynamic equilibrium of MT polymerization and depolymerization. Presently, in material—protein interaction molecular dynamics simulations, it is common to propose *in silico* predictions and theoretical descriptions of molecular mechanisms based on structural properties and energy calculations. However, these theoretical possibilities are often rarely verified in real cells or proteins[56]. In this study, we went beyond proposing a new theory of the interaction between Au-rGO and MTs/tubulins *in silico* and conducted various *in vitro* experiments to experimentally validate our theoretical findings, which represent an important novelty of our research.

Firstly, using TEM, we observed Au-rGO in the cytoplasm 1 h after exposure (Fig. 6A), which supports that Au-rGO comes into direct contact with dissociated tubulin dimers and MTs. To elucidate the cellular entry mechanisms of Au-rGO, we conducted further examination of TEM images, which revealed the presence of both membrane-encapsulated particles and Au-rGO localized directly in the cytoplasm without membrane enclosure (Supporting Information Fig. S11A). To distinguish between different uptake pathways, cells were treated with sodium azide (20 μmol/L)—an inhibitor of energy-dependent endocytosis—along with Au-rGO exposure[57]. Intracellular gold content was quantified using ICP-MS. The inhibitor-treated group exhibited approximately 30% reduction in Au-rGO uptake compared to the Au-rGO-only group (Fig. S11B). These findings confirm that Au-rGO enters endothelial cells through both energy-dependent endocytosis and direct internalization. Once internalized, Au-rGO facilitates the opening of the BBB.

Next, drawing upon relevant studies on protein adsorption by nanomaterials[32,33], we developed an enhanced protein pull-down experiment to determine whether Au-rGO could interact with dissociated tubulin dimers and MTs, as illustrated in Fig. 6B (a). We exposed Au-rGO either to cells and then lysed the cells (sample 1) or to post-lysed cell lysate (sample 2). As a negative control, agarose beads were added to the cell lysate to ensure that no nonspecific proteins were pulled down during the experimental process (sample 3). In addition, agarose beads combined with α-tubulin or β-tubulin antibodies were used as a positive control (sample 4). The proteins bound to Au-rGO, if any, were "pulled down" by centrifugation and eluted. Equal volumes of eluates from all four samples were subjected to SDS-PAGE and subsequently examined using Coomassie blue staining (to identify proteins present in the eluate) and WB (to detect tubulin in the eluate). The results showed that both α-tubulin and β-tubulin were pulled down by Au-rGO (Fig. 6B (b)). In sample 1, tubulins pulled down could originate from both dissociated tubulin dimers and MTs. In contrast, sample 2, where Au-rGO was exposed only to dissociated tubulin dimers in the absence of assembled MTs, showed a greater amount of tubulins pulled down compared to sample 1 (Fig. 6C), confirming that Au-rGO predominantly adsorbs dissociated tubulin dimers in the cytoplasm, with minimal binding to assembled MTs; Otherwise, there would be no significant difference in tubulin levels between sample 1 and sample 2.

We further investigated the effects of Au-rGO on dissociated tubulin dimers and assembled MTs using a "Tubulin Polymerization Assay Kit", which uses highly purified tubulins to polymerize into MTs under controlled conditions. This kit incorporates

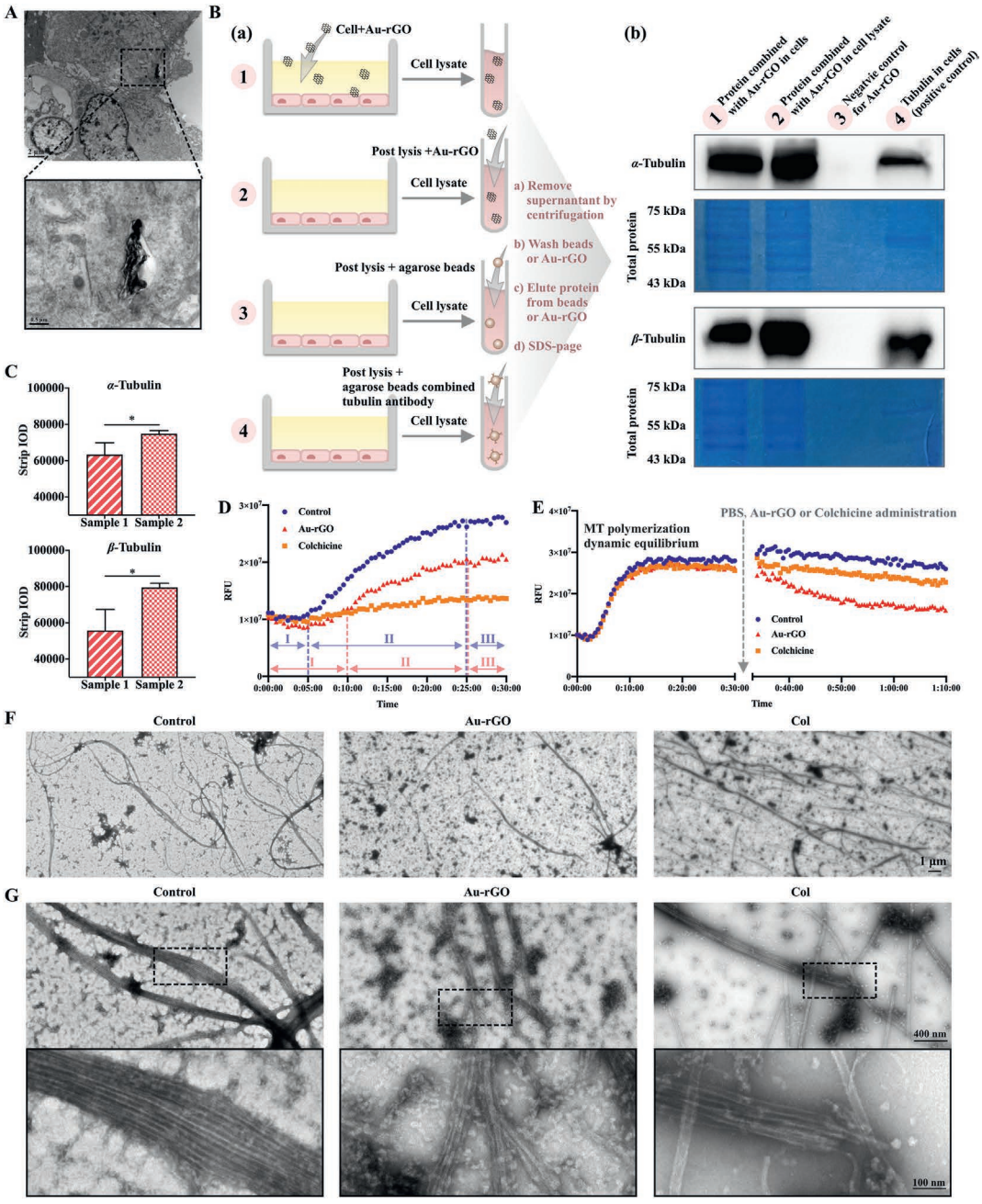

Figure 6 Au-rGO adsorbs dissociated tubulin dimers and induces assembled MTs to depolymerize. (A) TEM images of HCMEC/D3 cells exposed to 20 μg/mL Au-rGO for 1 h. The down panel shows an enlargement of the MTs in the box of the up panel. Scale bar: 2 μm in main images; 0.5 μm in zoomed images. (B) Schematic diagram of the modified protein pull-down assay (a) and immunoblot detection of α-tubulin and β-tubulin pulled by Au-rGO from cells and cell lysate (b). (C) Quantification and comparison of α-tubulin and β-tubulin pulled down by Au-rGO from cells and cell lysate using the strip integral optical density value, as there is no internal reference protein in this experiment. Data are represented as the mean ± SD ($n = 3$) $^*P < 0.05$ compared between the two groups. (D) Tubulin polymerization curves under the exposure of Au-rGO and Col added when the system contained only dissociated tubulins. Phase I-nucleation, Phase II-growth, and Phase III-steady-state equilibrium. (E) MTs' depolymerization curves under the exposure of Au-rGO and Col added after MT polymerization had reached dynamic equilibrium. Phase I-nucleation, Phase II-growth, and Phase III-steady-state equilibrium. (F) TEM images under low-power fields of purified MTs under the exposure of Au-rGO and Col. Scale bar: 1 μm. (G) TEM images obtained under high-power fields of purified MTs under the exposure of Au-rGO and Col. Scale bar: 400 nm in main images; 100 nm in zoomed images.

a fluorescent reporter into the MTs during polymerization, allowing us to monitor MT polymerization status through changes in fluorescence intensity measured by a fluorimeter. To examine the impact of Au-rGO on dissociated tubulin dimers, Au-rGO and Col (used as a positive control) were added from the outset when the system contained only dissociated tubulins. Given that the kinetics of MT nucleation and elongation are highly sensitive to the concentration of soluble tubulins[58], the adsorption of soluble

dissociated tubulins by Au-rGO in the cytoplasm should impede MT polymerization. This hypothesis can indeed be confirmed by observed results: the standard polymerization curve (control group) showed three phases: nucleation (Phase I), growth (Phase II), and a steady equilibrium (Phase III) (Fig. 6D, blue curve); Au-rGO prolonged the nucleation phase, delayed the growth phase, reduced the polymerization rate, and decreased the fluorescence level during the steady phase (Fig. 6D, red curve). These results suggest that Au-rGO interfered with the polymerization of dissociated tubulins into MTs. In contrast, Col completely inhibited tubulin polymerization (Fig. 6D, orange curve).

To investigate the effects of Au-rGO on assembled MTs, Au-rGO and Col were added after MT polymerization had reached dynamic equilibrium. The control group's curve exhibited a slight disturbance upon the addition and mixing of PBS, but quickly returned to equilibrium (Fig. 6E, blue curve). Col induced a slight reduction in fluorescence compared to the control group, with overall equilibrium remaining largely unchanged compared to the addition of PBS (Fig. 6E, orange curve), which aligns with the knowledge that Col preferentially binds soluble dissociated tubulin to hinder MT polymerization but does not disassemble MTs into monomers[59]. In contrast, the fluorescence level in the presence of Au-rGO gradually decreased over time, and the reduction was much greater than that induced by Col (Fig. 6E, red curve), suggesting that MTs not only struggled to maintain polymerization but also underwent significant depolymerization.

Finally, we visually illustrated the changes in MTs exposed to Au-rGO and Col through TEM, a first-of-its-kind observation to our knowledge. Purified tubulin was first polymerized, and then PBS, Au-rGO, or Col was added to the system for 30 min, and the samples were observed through TEM after negative staining. TEM images under low-power fields revealed distinct differences in the appearance of MTs (Fig. 6F): MTs in the control group appeared long and smooth, while those in the Au-rGO group were considerably shorter and less abundant; comparatively, MTs in the Col group exhibited significant fractures. TEM images obtained under high-power fields showed that Au-rGO induced MT bundles to separate, resulting in a distinct gap between the MTs, while MTs in the Col group displayed bending and broken ends (Fig. 6G). These observed changes align with the alterations in MT structure we previously observed in cells using IF, whereby Au-rGO led to a uniform blurring of tubulin staining, while Col induced partial spot-like highlighting of MTs.

Collectively, our comprehensive approach, combining molecular dynamics simulation with a series of cell and protein experiments, confirmed the subtle molecular mechanism of the interaction between Au-rGO and MTs: Au-rGO adsorbs dissociated tubulins, hindering MT polymerization and concurrently acts on assembled MTs to promote depolymerization.

3.6. MT polymerization is responsible for the recovery of the BBB

Although the opening of the paracellular route in the BBB holds great promise for enhanced drug delivery, this route should effectively close promptly to prevent adverse effects, such as inflammation and edema[18]. Therefore, when investigating nanomaterials for opening the BBB, it is equally important to understand the mechanism of its closure. In our previous *in vitro* experiments, we observed a recovery in MT polymerization between 2 and 6 h following Au-rGO exposure. As the initial disruption of the BBB is linked to MT depolymerization, we hypothesized that the subsequent recovery might involve MTs resuming polymerization. To test this, we used Col to interfere with MT polymerization during the 2−6-h period after Au-rGO exposure (grouping outlined in Fig. 7A) and assessed BBB status. WB analysis confirmed MT polymerization status, revealing that Col added 2 h after Au-rGO exposure impeded the resurgence of MT polymerization (Fig. 7B). Then we found that the TEER value and Na-Flu permeability changed first (compare sample 1 and sample 2) and had recovered by 6 h after Au-rGO exposure (compare sample 1 and sample 3); however, inhibiting MT polymerization with Col prevented this recovery (compare sample 3 and sample 4) (Fig. 7C and D). We also evaluated AJ and TJ protein levels on the cell membrane. WB results (Fig. 7E and F) and IF images (Fig. 7G and H) demonstrated that inhibiting MT polymerization hindered the restoration of AJ and TJ protein levels on the cell membrane. These findings strongly support that MTs play a central role in regulating Au-rGO-induced paracellular permeability in the BBB and that the closure of the BBB at the later stage (2−6 h) can be attributed to MT polymerization.

Considering that Au-rGO direct interaction with MTs or dissociated tubulins both induced depolymerization of MTs, we proposed that MT polymerization is likely stimulated through the activation of signaling pathways rather than direct Au-rGO interaction. To identify potentially involved signaling pathways, we conducted RNA sequencing on cells exposed to Au-rGO for 2 h, coinciding with the onset of MT polymerization. Kyoto Encyclopedia of Genes and Genomes analysis indicated the enrichment of certain differentially expressed genes in the MAPK signaling pathway (Fig. 8A). Furthermore, Gene Ontology enrichment analysis revealed enrichment in the ERK cascade among the differentially expressed genes (Fig. 8B). Upon reviewing the literature, we found that ERK can modulate the binding and release of free tubulin by phosphorylating stathmin, thereby regulating MT polymerization[60,61], as shown in Fig. 8C. Herein, phosphorylation of ERK and stathmin was observed starting from 2 h, with a significant increase at 6 h (Fig. 8D). Concurrently, we examined the amount of tubulin bound to stathmin through Co-IP. We observed a reduction in tubulin−stathmin binding at 2 h, with a more substantial reduction at 6 h (Fig. 8E). Additionally, when ERK was inhibited by an ERK inhibitor during the later stage (2−6 h) of Au-rGO exposure (grouping outlined in Supporting Information Fig. S12A), stathmin phosphorylation decreased (Fig. S12B), and the level of soluble tubulin significantly increased (Fig. 8F). These results confirmed that ERK activation induced stathmin phosphorylation, leading to tubulin release and promoting MT polymerization. Moreover, the addition of the ERK inhibitor resulted in a significant reduction in TEER and a marked increase in Na-Flu permeability (Fig. 8G and H). Levels of AJ and TJ proteins also decreased, as shown in Fig. S12C−S12G. These parameters reflecting BBB paracellular permeability indicated that inhibiting ERK during the later stage impeded BBB recovery, which collectively supports the conclusion that BBB integrity recovers due to MT polymerization regulated by the ERK−stathmin pathway.

But how does Au-rGO directly trigger ERK phosphorylation? Our earlier research has shown that GBMs can activate the ERK signaling pathways *via* the upstream Raf−MEK cascade —a classical axis typically associated with apoptosis regulation, often in response to oxidative stress from intracellular ROS accumulation[62,63]. However, in the present study, we detected no significant activation of Raf or MEK at the time points corresponding to peak ERK phosphorylation (Supporting Information Fig. S13A), nor did we observe any increase in intracellular ROS (Fig. S8B).

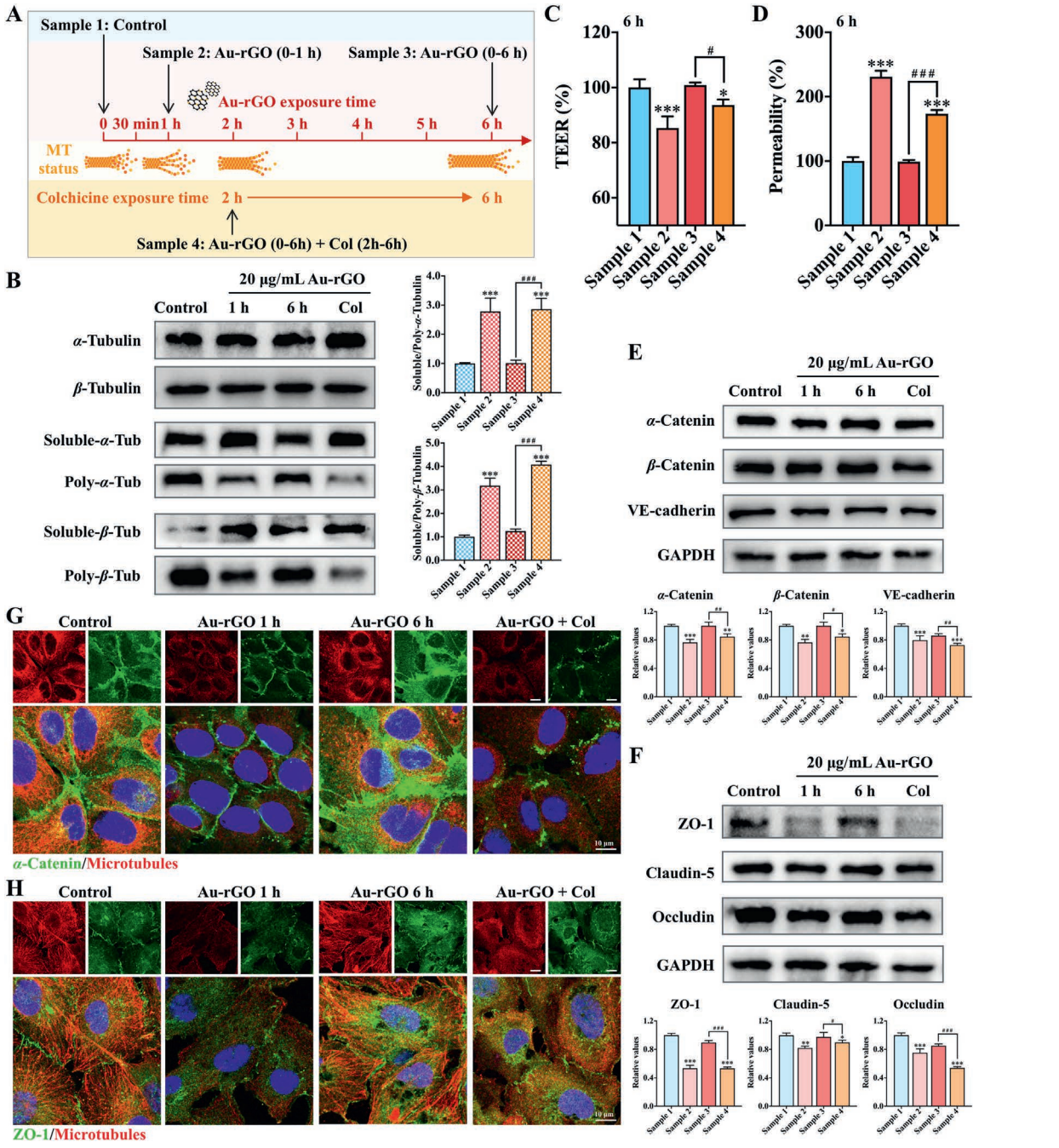

Figure 7 MT polymerization mediates the recovery of the BBB. (A) Illustration of grouping: Sample 1 is the control group; Sample 2 is cells exposed to 20 μg/mL Au-rGO for 1 h; Sample 3 is cells exposed to 20 μg/mL Au-rGO for 6 h; Sample 4 is cells exposed to 20 μg/mL Au-rGO for 6 h, with Col to block tubulin polymerization from 2 to 6 h. (B) Immunoblot analysis of total, soluble, and polymerized α-tubulin and β-tubulin in various samples. (C) TEER values of different samples. (D) Na-Flu permeability results for different samples. (E, F) Immunoblot analysis of AJ (E) and TJ (F) proteins in different samples. (G, H) Immunostaining of HCMEC/D3 cells for α-catenin (G) and ZO-1 (H) (green), MTs (red), and cell nuclei (blue). Scale bar: 10 μm. Data are represented as the mean ± SD ($n = 3$). *$P < 0.05$, **$P < 0.01$, and ***$P < 0.001$ compared with the control group. $^{\#}P < 0.05$, $^{\#\#}P < 0.01$ and $^{\#\#\#}P < 0.001$ compared between the two experiment groups.

These results suggest that Au-rGO-induced ERK activation occurs independently of both oxidative stress and the canonical Raf−MEK−ERK pathway. Since ERK activation—which regulates MT polymerization—occurred between 2 and 6 h and was more pronounced at 6 h, we concluded that it is unlikely to be caused by directly internalized Au-rGO. Instead, we propose that internalized Au-rGO undergoes intracellular processing before triggering ERK signaling. This hypothesis is supported by our observation that inhibiting endocytosis nearly completely abolished ERK activation (Fig. S13B). It's known that endocytosed GBMs traffic through endosomal and lysosomal compartments, where it is fragmented into smaller nanosheets by enzymes and a low pH environment before escaping into the cytoplasm[64,65]. We hypothesize that these resulting fragments or intermediate

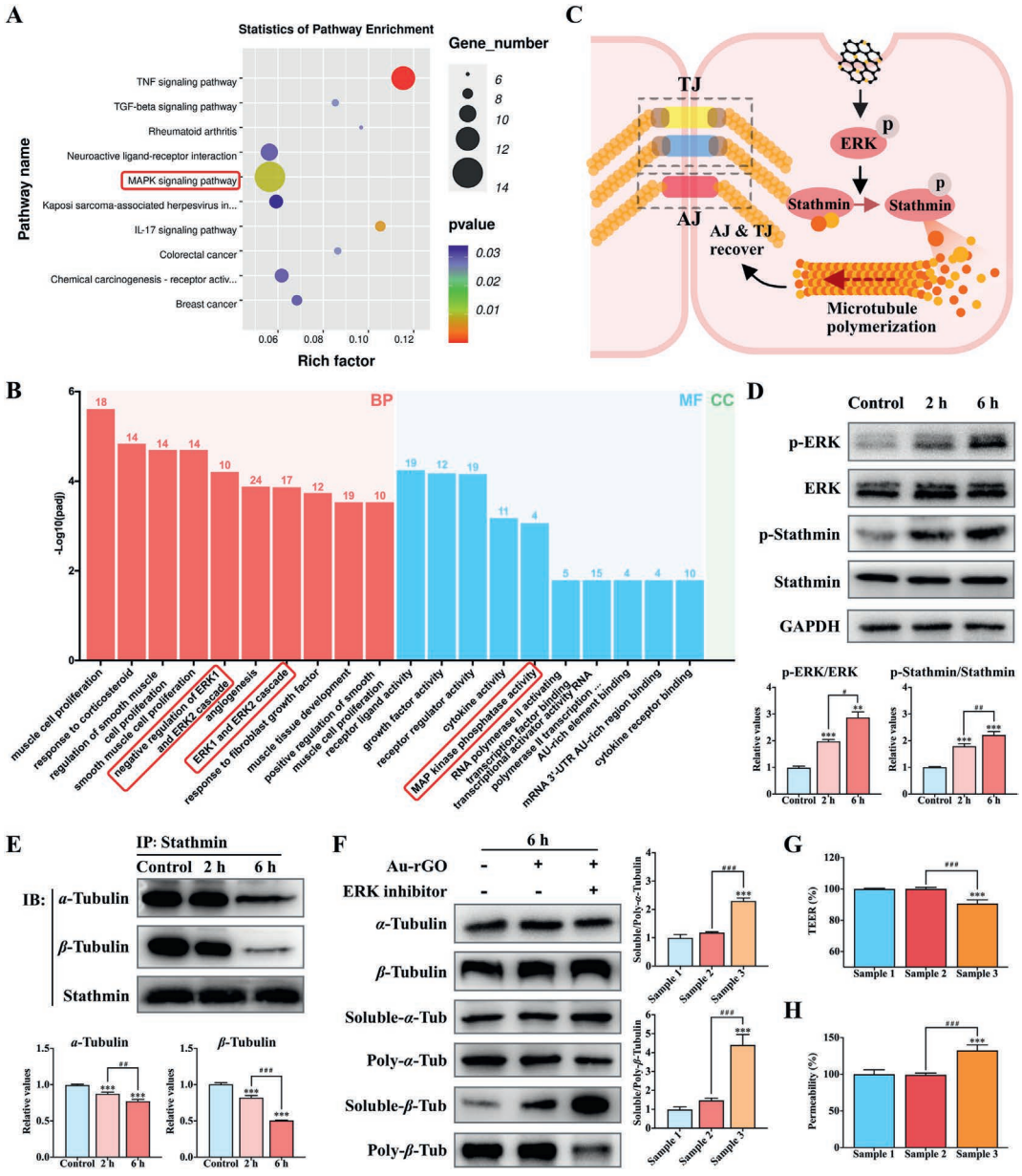

Figure 8 The mechanism of Au-rGO induces MT polymerization at a later stage of exposure. (A) Signaling pathways enriched with differentially expressed genes, analyzed by Kyoto Encyclopedia of Genes and Genomes analysis, with the MAPK signaling pathway showing the most enrichment. (B) Gene Ontology analysis highlighting differential gene enrichment in "Biological Process" (red column) and "Molecular Function" (blue column), with no enrichment in "Cellular Component." Most differential genes are associated with ERK-related cascades. (C) Illustration of the process by which the ERK−stathmin pathway regulates MT polymerization. (D) Immunoblot analysis of phosphorylated ERK and stathmin in HCMEC/D3 cells exposed to 20 μg/mL Au-rGO for 2 and 6 h. (E) Co-immunoprecipitation of proteins from HCMEC/D3 cells exposed to 20 μg/mL Au-rGO for 2 and 6 h using stathmin antibody, followed by detection of captured stathmin and associated tubulins using WB assays. (F) Immunoblot detection of total, soluble, and polymerized α-tubulin and β-tubulin in HCMEC/D3 cells exposed to 20 μg/mL Au-rGO for 6 h or with ERK inhibitor exposure from 2 to 6 h. (G) TEER value of different samples. (H) Na-Flu permeability results for different samples. Data are represented as the mean ± SD ($n = 3$). $^{*}P < 0.05$, $^{**}P < 0.01$, and $^{***}P < 0.001$ compared with the control group. $^{\#}P < 0.05$, $^{\#\#}P < 0.01$ and $^{\#\#\#}P < 0.001$ compared between the two experiment groups.

degradation products are responsible for ERK activation. To test this, we employed a calcein-based endosomal leakage assay[66]. Calcein, a membrane-impermeable fluorescent dye, is passively internalized *via* micropinocytosis and accumulates in endolysosomal compartments, where its fluorescence is self-quenched under acidic conditions. Nanomaterial-induced lysosomal membrane disruption leads to calcein release into the cytosol, resulting in bright, diffuse fluorescence (Fig. S13C (a)). Our results showed that Au-rGO induced the release of calcein into the cytosol, producing strong and diffuse fluorescence, confirming endolysosomal escape (Fig. S13C (b)). Next, we employed Bafilomycin A1 (50 nmol/L) to alkalize the lysosomal acidic environment (Fig. S13D) and found that this treatment markedly inhibited ERK phosphorylation (Fig. S13E). Collectively, these findings support a

mechanism where acidic lysosomal conditions and enzymatic activity promote the hydrolysis and fragmentation of Au-rGO, generating smaller nanosheets or bioactive intermediates that, upon cytosolic release, facilitate ERK activation and eventually ensure the timely closure of the paracellular route in the opened BBB. This mechanism serves as a critical foundation for the safe and effective use of Au-rGO as a paracellular permeability enhancer, ultimately enhancing BBB drug delivery efficiency.

Herein, we demonstrated that Au-rGO achieves reversible BBB opening by modulating MT dynamics, specifically through depolymerization (barrier opening stage) and polymerization (barrier resealing) processes. Unlike nanomaterials requiring additional modifications (*e.g.*, with borneol[67], adenosine[68], etc.), Au-rGO inherently possesses BBB-opening capability. Compared to reported metal-oxide nanoparticles that open the BBB by directly compromising cell viability and junction protein expression[69], Au-rGO exhibits lower cytotoxicity and offers a more controlled BBB-opening time window. Relative to traditional non-nano paracellular enhancers—such as hyperosmotic agents (*e.g.*, mannitol[70]), biological compounds (*e.g.*, bradykinin[71]), and chemical permeation enhancers (*e.g.*, sodium dodecyl sulfate[72])—Au-rGO can be functionally modified and drug-loaded, while posing significantly lower risks of water/electrolyte imbalances and allergic reactions at effective doses. This demonstrates that Au-rGO is an ideal paracellular penetration enhancer.

Further, through *in vivo* and *in vitro* experiments demonstrating the reversible opening of the BBB by Au-rGO, we have revealed the tip of the iceberg regarding the mechanism of action between GBMs and the BBB. Numerous other studies have shown that GBMs can serve as ideal drug carriers, or even as platforms integrating multiple therapeutic approaches[23,73,74]. Our research further confirms that GBMs can also function as safe BBB-opening modulators. To use a metaphor, GBMs act like a versatile therapeutic agent capable of multiple roles, and we now discover they also possess the "key" to open the BBB. Consequently, when developing graphene-based therapeutics for neurological diseases, there might not be a need to incorporate an additional penetration enhancer specifically for BBB opening. Specifically for treating brain tumors such as glioma and brain metastases[75], utilizing GBMs as carriers allows for the focused functionalization with chemotherapeutic agents, tumor-targeting molecules, and molecules facilitating adjunctive photothermal/photodynamic therapy—without the need to specifically functionalize them for BBB opening[17,21]. This approach enhances functionalization efficiency and reduces complexity in material preparation.

4. Conclusions

In summary, we comprehensively investigated the impact of Au-rGO, a type of GBM, on the BBB through *in vivo* and *in vitro* experiments, as well as *in silico* simulations, which revealed that Au-rGO can rapidly and reversibly open the paracellular route of the BBB by modulating the polymerization and depolymerization dynamics of MTs within cerebral vascular endothelial cells. Importantly, we elucidated and validated that Au-rGO influences MT dynamic equilibrium through two distinct mechanisms: the adsorption of soluble dissociated tubulins within the cytoplasm to impede MT polymerization and the application of forces on assembled MTs to induce depolymerization. Furthermore, we observed that the later closure of the BBB, which was mediated by increased MT polymerization, was regulated by the activation of the ERK−stathmin pathway. Our findings significantly contribute to a deeper understanding of the mechanisms underlying the reversible opening of the BBB by GBMs. Moreover, we provide experimental evidence supporting the use of Au-rGO as a safe and effective paracellular penetration enhancer, with the potential to enhance the efficiency of drug delivery across the BBB.

Acknowledgments

This work was supported by the National Natural Science Foundation of China (82101695, 82472126, and 82172079), the China Postdoctoral Science Foundation (2024M761346), the Special research project of post-marketing clinical research of innovative drugs (WKZX2023CX060001, China), the R&D Program of Guangzhou National Laboratory (GZNL2023A03001, China). We thank the Home for Researchers editorial team (www.home-for-researchers.com) for language editing service.

Author contributions

Junrong Wu: Conceptualization, Writing − original draft, Funding acquisition. Guangman Cui: Data curation, Writing − review and editing. Zhousheng Lin: Data curation. Wanmei Lin: Formal analysis. Yaqing Zhang: Data curation. Tianhang Zhou: Software. Ping He: Supervision. Yunjiao Zhang: Supervision, Writing − review and editing. Guangyu Yao: Supervision, Funding acquisition.

Conflicts of interest

The authors reported no potential conflicts of interest.

Appendix A. Supporting information

Supporting information to this article can be found online at https://doi.org/10.1016/j.apsb.2025.12.015.

References

1. Kadry H, Noorani B, Cucullo L. A blood−brain barrier overview on structure, function, impairment, and biomarkers of integrity. *Fluids Barriers CNS* 2020;**17**:69.
2. Terstappen GC, Meyer AH, Bell RD, Zhang W. Strategies for delivering therapeutics across the blood−brain barrier. *Nat Rev Drug Discov* 2021;**20**:362−83.
3. Pawar B, Vasdev N, Gupta T, Mhatre M, More A, Anup N, et al. Current update on transcellular brain drug delivery. *Pharmaceutics* 2022;**14**:2719.
4. Furtado D, Bjornmalm M, Ayton S, Bush AI, Kempe K, Caruso F. Overcoming the blood−brain barrier: the role of nanomaterials in treating neurological diseases. *Adv Mater* 2018;**30**:e1801362.
5. Pietroiusti A, Campagnolo L, Fadeel B. Interactions of engineered nanoparticles with organs protected by internal biological barriers. *Small* 2013;**9**:1557−72.
6. Reddy S, Tatiparti K, Sau S, Iyer AK. Recent advances in nano delivery systems for blood−brain barrier (BBB) penetration and targeting of brain tumors. *Drug Discov Today* 2021;**26**:1944−52.
7. Han L, Jiang C. Evolution of blood−brain barrier in brain diseases and related systemic nanoscale brain-targeting drug delivery strategies. *Acta Pharm Sin B* 2021;**11**:2306−25.
8. McLoughlin CD, Nevins S, Stein JB, Khakbiz M, Lee KB. Overcoming the blood−brain barrier: multifunctional nanomaterial-based

strategies for targeted drug delivery in neurological disorders. *Small Sci* 2024;**4**:2400232.
9. Li M, Zhang W, Li J, Qi Y, Peng C, Wang N, et al. Zwitterionic polymers: addressing the barriers for drug delivery. *Chin Chem Lett* 2023;**34**:108177.
10. Guo S, Li C, Wang C, Cao X, Liu X, Liang XJ, et al. pH-Responsive polymer boosts cytosolic siRNA release for retinal neovascularization therapy. *Acta Pharm Sin B* 2024;**14**:781−94.
11. Xie C, Liao J, Zhang N, Sun Y, Li Y, Xiong L, et al. Advanced nano drug delivery systems for neuroprotection against ischemic stroke. *Chin Chem Lett* 2024;**35**:109149.
12. Ji WH, Xiao ZB, Liu GY, Zhang X. Development and application of nano-flavor-drug carriers in neurodegenerative diseases. *Chin Chem Lett* 2017;**28**:1829−34.
13. Liang K, Yang L, Kang J, Liu B, Zhang D, Wang L, et al. Improving treatment for Parkinson's disease: harnessing photothermal and phagocytosis-driven delivery of levodopa nanocarriers across the blood−brain barrier. *Asian J Pharm Sci* 2024;**19**:100963.
14. Wei Y, Xia X, Wang X, Yang W, He S, Wang L, et al. Enhanced BBB penetration and microglia-targeting nanomodulator for the two-pronged modulation of chronically activated microglia-mediated neuroinflammation in Alzheimer's disease. *Acta Pharm Sin B* 2025;**15**:1098−111.
15. Salama NN, Eddington ND, Fasano A. Tight junction modulation and its relationship to drug delivery. *Adv Drug Deliv Rev* 2006;**58**:15−28.
16. Henna TK, Raphey VR, Sankar R, Ameena Shirin VK, Gangadharappa HV, Pramod K. Carbon nanostructures: the drug and the delivery system for brain disorders. *Int J Pharm* 2020;**587**:119701.
17. Razavi ZS, Razavi FS, Alizadeh SS. Inorganic nanoparticles and blood−brain barrier modulation: advancing targeted neurological therapies. *Eur J Med Chem* 2025;**287**:117357.
18. Wu J, Zhu Z, Liu W, Zhang Y, Kang Y, Liu J, et al. How nanoparticles open the paracellular route of biological barriers: mechanisms, applications, and prospects. *ACS Nano* 2022;**16**:15627−52.
19. Barani M, Mukhtar M, Rahdar A, Sargazi G, Thysiadou A, Kyzas GZ. Progress in the application of nanoparticles and graphene as drug carriers and on the diagnosis of brain infections. *Molecules* 2021;**26**:186.
20. Cui G, Wu J, Lin J, Liu W, Chen P, Yu M, et al. Graphene-based nanomaterials for breast cancer treatment: promising therapeutic strategies. *J Nanobiotechnol* 2021;**19**:211.
21. Shirvalilou S, Khoei S, Khoee S, Raoufi NJ, Karimi MR, Shakeri-Zadeh A. Development of a magnetic nano-graphene oxide carrier for improved glioma-targeted drug delivery and imaging: *in vitro* and *in vivo* evaluations. *Chem Biol Interact* 2018;**295**:97−108.
22. Xiong S, Luo J, Wang Q, Li Z, Li J, Liu Q, et al. Targeted graphene oxide for drug delivery as a therapeutic nanoplatform against Parkinson's disease. *Biomater Sci* 2021;**9**:1705−15.
23. Yu S, Wang X, Lv L, Liu T, Guan Q. Borneol-modified PEGylated graphene oxide as a nanocarrier for brain-targeted delivery of ginsenoside Rg1 against depression. *Int J Pharm* 2023;**643**:123284.
24. Perini G, Palmieri V, Ciasca G, D'Ascenzo M, Primiano A, Gervasoni J, et al. Enhanced chemotherapy for glioblastoma multiforme mediated by functionalized graphene quantum dots. *Materials* 2020;**13**:4139.
25. Huang X, Sheng B, Tian H, Chen Q, Yang Y, Bui B, et al. Real-time SERS monitoring anticancer drug release along with SERS/MR imaging for pH-sensitive chemo-phototherapy. *Acta Pharm Sin B* 2023;**13**:1303−17.
26. Castagnola V, Deleye L, Podesta A, Jaho E, Loiacono F, Debellis D, et al. Interactions of graphene oxide and few-layer graphene with the blood−brain barrier. *Nano Lett* 2023;**23**:2981−90.
27. Su S, Wang J, Qiu J, Martinez-Zaguilan R, Sennoune SR, Wang S. *In vitro* study of transportation of porphyrin immobilized graphene oxide through blood brain barrier. *Mater Sci Eng C Mater Biol Appl* 2020;**107**:110313.
28. Xiaoli F, Qiyue C, Weihong G, Yaqing Z, Chen H, Junrong W, et al. Toxicology data of graphene-family nanomaterials: an update. *Arch Toxicol* 2020;**94**:1915−39.
29. Kang Y, Liu J, Yin S, Jiang Y, Feng X, Wu J, et al. Oxidation of reduced graphene oxide *via* cellular redox signaling modulates actin-mediated neurotransmission. *ACS Nano* 2020;**14**:3059−74.
30. Bellier N, Baipaywad P, Ryu N, Lee JY, Park H. Recent biomedical advancements in graphene oxide- and reduced graphene oxide-based nanocomposite nanocarriers. *Biomater Res* 2022;**26**:65.
31. Putnam AJ, Cunningham JJ, Dennis RG, Linderman JJ, Mooney DJ. Microtubule assembly is regulated by externally applied strain in cultured smooth muscle cells. *J Cell Sci* 1998;**111**(Pt 22):3379−87.
32. Setyawati MI, Tay CY, Chia SL, Goh SL, Fang W, Neo MJ, et al. Titanium dioxide nanomaterials cause endothelial cell leakiness by disrupting the homophilic interaction of VE-cadherin. *Nat Commun* 2013;**4**:1673.
33. Huang Y, Wang S, Zhang J, Wang H, Zou Q, Wu L. Stealthy nanoparticles protect endothelial barrier from leakiness by resisting the absorption of VE-cadherin. *Nanoscale* 2021;**13**:12577−86.
34. Darabdhara G, Das MR, Singh SP, Rengan AK, Szunerits S, Boukherroub R. Ag and Au nanoparticles/reduced graphene oxide composite materials: synthesis and application in diagnostics and therapeutics. *Adv Colloid Interface Sci* 2019;**271**:101991.
35. Zhuo Q, Ma Y, Gao J, Zhang P, Xia Y, Tian Y, et al. Facile synthesis of graphene/metal nanoparticle composites *via* self-catalysis reduction at room temperature. *Inorg Chem* 2013;**52**:3141−7.
36. Yokel R, Grulke E, MacPhail R. Metal-based nanoparticle interactions with the nervous system: the challenge of brain entry and the risk of retention in the organism. *Wiley Interdiscip Rev Nanomed Nanobiotechnol* 2013;**5**:346−73.
37. Tan Q, Zhao S, Xu T, Wang Q, Lan M, Yan L, et al. Getting drugs to the brain: advances and prospects of organic nanoparticle delivery systems for assisting drugs to cross the blood−brain barrier. *J Mater Chem B* 2022;**10**:9314−33.
38. Ahishali B, Kaya M. Evaluation of blood−brain barrier integrity using vascular permeability markers: evans blue, sodium fluorescein, albumin-alexa fluor conjugates, and horseradish peroxidase. *Methods Mol Biol* 2021;**2367**:87−103.
39. Zwirner J, Lier J, Franke H, Hammer N, Matschke J, Trautz F, et al. GFAP positivity in neurons following traumatic brain injuries. *Int J Leg Med* 2021;**135**:2323−33.
40. Spadaro D, Le S, Laroche T, Mean I, Jond L, Yan J, et al. Tension-dependent stretching activates ZO-1 to control the junctional localization of its interactors. *Curr Biol* 2017;**27**:3783−95.e8.
41. Belardi B, Hamkins-Indik T, Harris AR, Kim J, Xu K, Fletcher DA. A weak link with actin organizes tight junctions to control epithelial permeability. *Dev Cell* 2020;**54**:792−804.e7.
42. Liu Y, Yoo E, Mahler GJ, Doiron AL. Endothelial barrier dysfunction induced by nanoparticle exposure through actin remodeling *via* caveolae/raft-regulated calcium signalling. *NanoImpact* 2018;**11**:82−91.
43. Snyder RJ, Hussain S, Rice AB, Garantziotis S. Multiwalled carbon nanotubes induce altered morphology and loss of barrier function in human bronchial epithelium at noncytotoxic doses. *Int J Nanomed* 2014;**9**:4093−105.
44. Wei Y, Zhou Y, Long C, Wu H, Hong Y, Fu Y, et al. Polystyrene microplastics disrupt the blood−testis barrier integrity through ROS-mediated imbalance of mTORC1 and mTORC2. *Environ Pollut* 2021;**289**:117904.
45. Alieva IB, Zemskov EA, Smurova KM, Kaverina IN, Verin AD. The leading role of microtubules in endothelial barrier dysfunction: disassembly of peripheral microtubules leaves behind the cytoskeletal reorganization. *J Cell Biochem* 2013;**114**:2258−72.
46. Vasileva E, Citi S. The role of microtubules in the regulation of epithelial junctions. *Tissue Barriers* 2018;**6**:1539596.
47. Karki P, Ke Y, Tian Y, Ohmura T, Sitikov A, Sarich N, et al. Staphylococcus aureus-induced endothelial permeability and inflammation are mediated by microtubule destabilization. *J Biol Chem* 2019;**294**:3369−84.

48. Setyawati MI, Mochalin VN, Leong DT. Tuning endothelial permeability with functionalized nanodiamonds. *ACS Nano* 2016;**10**: 1170−81.
49. Ratnikova TA, Govindan PN, Salonen E, Ke PC. *In vitro* polymerization of microtubules with a fullerene derivative. *ACS Nano* 2011;**5**: 6306−14.
50. Apopa PL, Qian Y, Shao R, Guo NL, Schwegler-Berry D, Pacurari M, et al. Iron oxide nanoparticles induce human microvascular endothelial cell permeability through reactive oxygen species production and microtubule remodeling. *Part Fibre Toxicol* 2009;**6**:1.
51. Zhou P, Yang G, Xie W. Organization of cortical microtubules in differentiated cells. *J Cell Physiol* 2023;**238**:1141−7.
52. Dzaki N, Bu S, Lau SSY, Yong WL, Yu F. Drosophila GSK3beta promotes microtubule disassembly and dendrite pruning in sensory neurons. *Development* 2022;**149**:dev200844.
53. Cappelletti G, Calogero AM, Rolando C. Microtubule acetylation: a reading key to neural physiology and degeneration. *Neurosci Lett* 2021;**755**:135900.
54. Selvaraj C, Sakkiah S, Tong W, Hong H. Molecular dynamics simulations and applications in computational toxicology and nanotoxicology. *Food Chem Toxicol* 2018;**112**:495−506.
55. Luan B, Cheng S. Potential interference with microtubule assembly by graphene: a tug-of-war. *Nanoscale* 2020;**12**:4968−74.
56. Ozboyaci M, Kokh DB, Corni S, Wade RC. Modeling and simulation of protein-surface interactions: achievements and challenges. *Q Rev Biophys* 2016;**49**:e4.
57. Rennick JJ, Johnston APR, Parton RG. Key principles and methods for studying the endocytosis of biological and nanoparticle therapeutics. *Nat Nanotechnol* 2021;**16**:266−76.
58. Brouhard GJ, Rice LM. Microtubule dynamics: an interplay of biochemistry and mechanics. *Nat Rev Mol Cell Biol* 2018;**19**:451−63.
59. Sebastian J, Rathinasamy K. Microtubules and cell division: potential pharmacological targets in cancer therapy. *Curr Drug Targets* 2023; **24**:889−918.
60. Filbert EL, Le Borgne M, Lin J, Heuser JE, Shaw AS. Stathmin regulates microtubule dynamics and microtubule organizing center polarization in activated T cells. *J Immunol* 2012;**188**:5421−7.
61. Szyk A, Piszczek G, Roll-Mecak A. Tubulin tyrosine ligase and stathmin compete for tubulin binding *in vitro*. *J Mol Biol* 2013;**425**: 2412−4.
62. Kang Y, Liu J, Wu J, Yin Q, Liang H, Chen A, et al. Graphene oxide and reduced graphene oxide induced neural pheochromocytoma-derived PC12 cell lines apoptosis and cell cycle alterations *via* the ERK signaling pathways. *Int J Nanomed* 2017;**12**:5501−10.
63. Li S, Chen J, Fan Y, Wang C, Wang C, Zheng X, et al. Liposomal Honokiol induces ROS-mediated apoptosis *via* regulation of ERK/p38-MAPK signaling and autophagic inhibition in human medulloblastoma. *Signal Transduct Targeted Ther* 2022;**7**:49.
64. Peng Z, Liu X, Zhang W, Zeng Z, Liu Z, Zhang C, et al. Advances in the application, toxicity and degradation of carbon nanomaterials in environment: a review. *Environ Int* 2020;**134**:105298.
65. Cupic KI, Rennick JJ, Johnston AP, Such GK. Controlling endosomal escape using nanoparticle composition: current progress and future perspectives. *Nanomedicine (Lond)* 2019;**14**:215−23.
66. Smith SA, Selby LI, Johnston APR, Such GK. The endosomal escape of nanoparticles: toward more efficient cellular delivery. *Bioconjug Chem* 2019;**30**:263−72.
67. Wu X, Yuan R, Xu Y, Wang K, Yuan H, Meng T, et al. Functionalized lipid nanoparticles modulate the blood−brain barrier and eliminate alpha-synuclein to repair dopamine neurons. *Asian J Pharm Sci* 2024; **19**:100904.
68. Meng L, Wang C, Lu Y, Sheng G, Yang L, Wu Z, et al. Targeted regulation of blood−brain barrier for enhanced therapeutic efficiency of hypoxia-modifier nanoparticles and immune checkpoint blockade antibodies for glioblastoma. *ACS Appl Mater Interfaces* 2021;**13**: 11657−71.
69. Kim EH, Baek SM, Kim D, Choi S, Kim W, Bian Y, et al. Iron overload and oxidative stress participated in zinc oxide nanoparticles-induced blood−brain barrier dysfunction. *Ecotoxicol Environ Saf* 2025;**301**:118528.
70. Le TN, Blakley BW. Mannitol and the blood-labyrinth barrier. *J Otolaryngol Head Neck Surg* 2017;**46**:66.
71. Al-Ahmad AJ, Pervaiz I, Karamyan VT. Neurolysin substrates bradykinin, neurotensin and substance P enhance brain microvascular permeability in a human *in vitro* model. *J Neuroendocrinol* 2021;**33**: e12931.
72. Saija A, Princi P, Trombetta D, Lanza M, De Pasquale A. Changes in the permeability of the blood−brain barrier following sodium dodecyl sulphate administration in the rat. *Exp Brain Res* 1997;**115**: 546−51.
73. Zhang J, Zhu S, Jin P, Huang Y, Dai Q, Zhu Q, et al. Graphene oxide improves postoperative cognitive dysfunction by maximally alleviating amyloid beta burden in mice. *Theranostics* 2020;**10**: 11908−20.
74. Wang Y, Wang K, Zhao J, Liu X, Bu J, Yan X, et al. Multifunctional mesoporous silica-coated graphene nanosheet used for chemo-photothermal synergistic targeted therapy of glioma. *J Am Chem Soc* 2013;**135**:4799−804.
75. Rijmers J, Lebre MC, Beijnen JH, Schinkel AH. Resistance mutations and the blood−brain barrier: key challenges in targeted treatment of brain metastatic non-small cell lung cancer. *Acta Pharm Sin B* 2025; **15**:3833−51.